

Journal Pre-proof

Fast nonlinear mechanical features decoupling to identify and predict asphalt-based composites

Z. Dai, V. Laheri, X. Zhu, F.A. Gilabert



PII: S0020-7403(22)00223-5
DOI: <https://doi.org/10.1016/j.ijmecsci.2022.107309>
Reference: MS 107309

To appear in: *International Journal of Mechanical Sciences*

Received date : 24 February 2022
Revised date : 19 April 2022
Accepted date : 19 April 2022

Please cite this article as: Z. Dai, V. Laheri, X. Zhu et al., Fast nonlinear mechanical features decoupling to identify and predict asphalt-based composites. *International Journal of Mechanical Sciences* (2022), doi: <https://doi.org/10.1016/j.ijmecsci.2022.107309>.

This is a PDF file of an article that has undergone enhancements after acceptance, such as the addition of a cover page and metadata, and formatting for readability, but it is not yet the definitive version of record. This version will undergo additional copyediting, typesetting and review before it is published in its final form, but we are providing this version to give early visibility of the article. Please note that, during the production process, errors may be discovered which could affect the content, and all legal disclaimers that apply to the journal pertain.

© 2022 Elsevier Ltd. All rights reserved.

Fast nonlinear mechanical features decoupling to identify and predict asphalt-based composites

Z. Dai^{a,b}, V. Laheri^b, X. Zhu^a and F. A. Gilabert^{b,*}

^aTongji University, Key Laboratory of Road and Traffic Engineering of the Ministry of Education, 4800 Cao'an Road, 201804 Shanghai, P.R. China

^bGhent University, Department of Materials, Textiles and Chemical Engineering, Tech Lane Ghent Science Park - Campus A, Technologiepark-Zwijnaarde 46, 9052 Zwijnaarde, Belgium.

ARTICLE INFO

Keywords:

Elasto-viscoplastic-viscodamage

Rate-dependency

Compression-tension asymmetry

Load-Unload-Reload

Optimization

Material parameter identification

ABSTRACT

Nonlinear matrices employed in asphalt-based composites exhibit a prominent nonlinear elasto-viscoplastic-viscodamageable mechanical response. The constitutive model for this type of matrices requires a significant experimental effort to identify the material constants. To alleviate the characterization effort without losing reliability in the mechanical prediction, this paper presents a fast procedure decoupling the elasto-viscoplastic response from the viscodamageable one and facilitating the identification of the material constants via efficient optimization. This procedure relies on a combined experimental-numerical also applicable to other rheologically complex materials like polyurea, thermoplastics or elasto-viscoplastic polycrystals. The experimental part is deliberately designed to only conduct cost- and time-effective *monotonic* loads at different strain rates in tension and compression. These pure monotonic results are used in the constitutive model to predict more complex loading conditions such as *multiple load-unload-reload* (LUR) cycles. To do this, an elasto-viscoplastic constitutive model suitable to describe creep-like phenomena and large irreversible deformations is proposed. This model incorporates pressure and strain rate sensitivity, which is essential to capture the compression-tension asymmetry in asphalt-based composites. A rate-dependent damage model is proposed to describe the degradation rate of the elasto-viscoplastic part. The stress and the consistent tangent modulus are derived. The model implementation for user-defined finite element subroutines are given for explicit or implicit solvers. The proposed decoupling facilitates an efficient identification of the constant parameters via an in-house Nelder-Mead-based optimization method. To accelerate the identification, all the stress-strain curves, either in tension or compression, are simultaneously used with applying physically-based constraints. The framework is validated with asphalt matrix at room temperature (24°C) and verified under LUR conditions at different rates. The identified model predicts correctly the experimental observations, proving its applicability to investigate particle-based composites with highly nonlinear matrices.


1. Introduction

Composites are widely used in different fields such as automobile, aerospace, medical, energy, civil or road engineering. Composites provide outstanding performance by combining several constituent materials with different but complementary mechanical behaviors.

For example, in sectors like aerospace or medicine, Fiber-Reinforced Polymers (FRP) are employed in lightweight structures like aero-elastic components or limb prostheses, respectively. They typically consist in glass or carbon fibers embedded in a polymer resin. This type of composites receives prominent attention due to its inherent high technological value. Therefore, these sectors heavily invest in computational methods like multiscale simulations that need reliable and efficient constitutive material models [1–4]. Another example can be found in a very different industrial sector such as road engineering, where asphalt concrete is used in pavement design. This composite is a three-phase composite consisting of asphalt matrix, coarse aggregate and air voids.

In the above examples, the properties of the constituent materials have in common many aspects, namely, very stiff and brittle reinforcement inclusions (fibers or stone aggregates) embedded in a highly nonlinear matrix (polymer or asphalt). This matrix is greatly affected by the loading and environmental conditions. It is worth mentioning that the

*Corresponding author. Tel.: +32 9 331 04 19.

 fran.gilabert@ugent.be (F. A. Gilabert)

ORCID(s):

Nomenclature

t	time	\mathbf{Q}	Eigen-decomposition transformation matrix
Δt	time increment	\mathbb{I}	4 th order identity tensor
$\boldsymbol{\sigma}$	Stress tensor	\mathbb{P}	4 th order projection tensor
$\boldsymbol{\varepsilon}$	Strain tensor	C_e	Consistent elastic tangent modulus
$\varepsilon_{\text{peak}}$	Strain occurring at peak stress value	C_{ep}	Consistent elastic-viscoplastic tangent modulus
a	Strain at peak index	C_1	Reference effective creep rate
Ω	Load direction dependent material coefficient	C_2	Relaxation kinetics coefficient
R^2	Coefficient of determination	m	Inelastic flow coefficient
P	Hydrostatic pressure	τ_B	Reference shear stress coefficient
$\boldsymbol{\sigma}'$	Deviatoric stress tensor	λ_{chain}	Inelastic network stretch
$\dot{\boldsymbol{\varepsilon}}$	Strain rate tensor	ξ	Pressure sensitivity coefficient
$\Delta \boldsymbol{\varepsilon}$	Strain increment tensor	ψ	Helmholtz free energy density
$\dot{\bar{\varepsilon}}$	Equivalent strain rate	ϕ	Yield function
$\dot{\varepsilon}_{\text{eff}}$	Effective strain rate	λ	Lamé's first parameter
τ	Equivalent shear stress	μ	Lamé's second parameter
\mathbf{I}	2 nd order identity tensor	Λ	Lagrange multiplier
\mathbf{F}	Total deformation gradient tensor	E	Young's modulus
\mathbf{F}_e	Elastic deformation gradient tensor	c_s	Speed of stress waves
\mathbf{F}_i	Inelastic deformation gradient tensor	l_{ele}	Characteristic length
\mathbf{D}	Rate of deformation tensor	d	Damage variable
\mathbf{W}	Spin tensor	\dot{d}	Instantaneous damage rate
\mathbf{L}	Velocity gradient tensor	\dot{d}_{∞}	Damage rate at infinity strain rate
\mathbf{N}	Direction tensor	ρ	Density
\mathbf{h}	Hencky strain tensor	η	Dimensionless damping coefficient
\mathbf{B}	Left Cauchy-Green deformation tensor	T	Temperature

technological level and costs involved for pavement design in road engineering differ substantially from those involved in aerospace or medical applications. Nevertheless, asphalt concrete is perhaps the most common composite in road engineering being absolutely crucial in the transportation infrastructures worldwide. Thus, this sector is also increasingly demanding simulation-based techniques to design new advanced and more efficient Asphalt-Based Composites (ABC).

Compared to FRP, the development of ABC involve more stringent conditions bounded by aspects like lower material's added value, simpler production technologies and cheaper costs of raw materials. In other words, the modeling effort must be even lower than that used in FRP composites. This means that, road engineering sector demands fast and very cost-effective numerical approaches in terms of easiness material parameter identification and reliability on capturing complex combinations of mechanical features. However, it must be noted that there is still a lack of understanding and efficient characterization of the asphalt matrix adapted to the requirements from this sector. On top of that, the asphalt matrix is, in turn, another composite material consisting of asphalt binder, fine aggregates and voids. This matrix is essentially the main source of nonlinearities in asphalt concrete, namely, rate- and pressure-dependent, thermo-sensitive, plastic, damageable and self-healable.

In terms of experimental characterization, researches usually study different loading conditions requiring large testing campaigns using complex instrumentation and specimen preparation. Additionally, it is common that these tests aim at researching the material response assuming non-coupled nonlinearities. For example, setups like Indirect Tension (IDT) [5], Semi-Circular Bending (SCB) [6] or Single-Edge Notched Beam (SENB) [7] are employ to study the fracture behavior of asphalt matrix similarly prepared and tested as asphalt concrete to visualize the fracture response.

However, from these tests is hard to quantify, for instance plasticity, load direction effects or rate-dependency. Other setups like Split Hopkinson Pressure Bar (SHPB) [8], Bending Beam Rheometer (BBR) [9], or modified Binder Bond Strength (BBS) [10] are used to study dynamic failure, matrix-aggregate interface adhesion-decohesion, micro-crack evolution or moisture damage. Again, these tests pose experimental difficulties to reveal the nonlinear role of the matrix in the overall ABC response. Recent research relied on Dynamic Mechanical Analyzer (DMA) [11] showing the strong rate-dependency and compression-tension asymmetry of asphalt matrix under quasi-static and dynamic conditions, although none damage effect was reported.

From the simulation point of view, once a constitutive material model is formulated based on experimental observations, test data are required to identify the model parameters. After that, the model must demonstrate to capture correctly the response under conditions not used during the identification. Considering the complex nonlinearities present in materials like ABC, the time and costs required for a full testing campaign in road engineering would be unacceptable. Thus, this research has selected the asphalt matrix to develop a pragmatic and cost-effective framework to overcome this situation. This approach might shed some inspiration to be applicable to other composites exhibiting coupling of similar nonlinearities. The novelties of the proposed approach rely on fulfilling the following requirements: (i) the specimens and test type must be easy to obtain and perform in an industrial environment, (ii) the constitutive model must be sufficiently realist without resorting to large and nonphysically-based parameters, (iii) the model construction allows the parameter identification process by decoupling nonlinearities, (iv) the identification process is fast and consistent with physical constrains and (v) the resulting identified model must be capable to predict more general loading scenarios not considered during identification.

Along with selecting the more convenient test typology for ABC, the modeling approach has to be chosen accordingly. In terms of asphalt-based constitutive modeling, three approaches can be adopted [12]. The *first* approach relies on the Boltzmann superposition integral mainly using the Schapery viscoelastic model [13, 14]. This consists in an integral-based form material model [15, 16] that can be enriched with nonlinear response like viscoplasticity [17] or aging [18, 19]. The *second* approach formulates the constitutive model considering the polymeric nature using a macromolecular description. Neilsen model [20, 21] and Lodge model [22] describe the deformation of polymer materials using the cross-linking, sliding, loosening and rearrangement behavior of the molecular network. Other nonlinearities like shear rate-dependent viscoelasticity [23–26], hydrolytic aging [27] or hardening [28] have also been studied. The *third* approach is termed as *differential* constitutive model consisting in assembling several rheological components such as Hookean springs (linear elasticity), Newtonian dashpot (linear viscosity), friction slider (plasticity), among many others. The way to assemble and activate the components give a wide flexibility to capture very different nonlinear response. Common examples used to predict viscoelastic response in asphalt-based materials are the Burgers model [29, 30], the three-element model [31], the generalized Maxwell model [11, 32, 33] or the generalized Kelvin-Voigt model [34]. Some researchers also added a rate-dependent plastic component to generate viscoelasto-plasticity [35–38]. The differential approach makes it possible to intuitively incorporate selected rheological components according to the observed tests results, therefore it is utilized in this work.

A crucial component to be used in this rheological assembly is damage. Continuum Damage Mechanics (CDM) is a well-established approach commonly used to describe material degradation in different simulation techniques like Finite Element Analysis (FEA), Discrete Element Method (DEM) [39, 40] or even Molecular Dynamics (MD) [41, 42]. CDM quantifies the effective surface of micro-cracks to degrade the material stiffness [43–45]. This approach can incorporate other effects such as moisture damage [46, 47] and combined with other nonlinearities like viscoelasticity and viscoplasticity [48–50]. Based on CDM, the Cohesive Zone Model (CZM) also enables to explicitly represent material discontinuities by using a traction-separation law at the crack lips [51–54]. More particularly, in ABC materials, CDM framework has been employed to develop the Fatigue damage theory [55–57], Glover-Rowe parameter [58] or Miner's rule [59, 60]. In this work a specific rheological model based on CDM will be proposed, which is constructed according to the experimental observations. This component will be coupled to the other rheological components to achieve mechanical consistency.

This paper presents a pragmatic framework combining an easy-to-test experimental setup with a flexible constitutive model providing reliable mechanical predictions for different loading scenarios. A novel optimization method based on the Nelder-Mead algorithm is developed to identify the model parameters using a minimum set of monotonic uniaxial tests. This algorithm fulfills physically-based user-defined constraints and uses a fast FEA-based single element test. The model construction along with the proposed identification process demonstrate that complex Load-Unload-Reload conditions can be accurately predicted. Although the constitutive model targets to ABC materials, slight model variations could cover other materials exhibiting asymmetric creep-like behavior such as polyurea [61],

Fast nonlinear mechanical decoupling for asphalt-based composites

Table 1

Three basic indices of asphalt binder.

Index	Test result	Grade
Penetration ($\times 10^{-1}$ mm)	60 ± 0.3	60 - 80
Softening point ($^{\circ}\text{C}$)	48.5 ± 0.25	44 - 54
Ductility at 10°C (cm)	> 150	> 100
Density (g/cm^3)	1.02 ± 0.03	-

Table 2

Gradation and aggregate density.

Aggregate size (mm)	Coarse aggregates					Fine aggregates					
	16	13.2	9.5	4.75	2.36	1.18	0.6	0.3	0.15	0.075	Pan
AC-13 Gradation (Retained percentage %)	0	4	23.1	32.31	9.84	8.04	7.35	4.1	3.54	2.21	5.5
Aggregate density (g/cm^3)						2.68	2.64	2.63	2.63	2.63	2.75

thermoplastics [62] or polycrystals [63].

This paper is organized as follows. In Section 2, the material composition, the specimen preparation and the test setup are described in detail. Section 3 introduces the experimental analysis of asphalt matrix. Section 4 and Section 5 present the proposed constitutive model and optimization method to identify its parameters, respectively, where the finite element software Abaqus [64] is used for the numerical simulations during optimization and verification. The discussion and conclusion of this study are finally summarized in the last two sections.

2. Experimental preparation

This section exposes the composition of the asphalt matrix and the fabrication process of the specimen for different tests, as well as the instrumentation and test setup.

2.1. Material composition

PEN 70 Asphalt binder and limestone aggregates are used to prepare the asphalt matrix in this study. The three basic indices and the density of the asphalt binder are tested and listed in Table 1.

Fine aggregates are defined by the Asphalt Institute (2001) [65] as the aggregates passing the 2.36 mm (No. 8) sieve. The total aggregates consist of 30.75 wt% fine aggregates (≤ 2.36 mm) and 69.25 wt% coarse aggregates (> 2.36 mm). The optimum asphalt-aggregate ratio of 4.5 wt% for AC-13 asphalt concrete is firstly obtained following the standard Marshall tests [66]. Based on that, the optimum asphalt-fine aggregate ratio is determined as $4.5/30.75 \times 100\% = 14.6\%$ for asphalt matrix.

The gradation and the density of fine aggregates are given in Table 2.

2.2. Specimen preparation and test setup

Taking into account the maximum aggregate size, the diameter of the specimen is determined as 10 mm. To prevent the buckling and barreling effects, the length of the specimen is determined as 20 mm and 40 mm for compression and tension tests, respectively. The cylindrical sample of asphalt matrix with the dimension of $\phi 150$ mm \times 60 mm is firstly prepared using a Superpave gyratory compactor (SGC, TIPTOP ICT-250) following the standard procedure in AASHTO T312 [67]. The upper and lower part of the sample are cut to ensure parallel and smooth surfaces. The remained cylindrical blocks with thicknesses of 20 mm and 40 mm for the compression and tension tests, respectively, are further processed. Small cylinder-shaped specimens with the aimed dimension of $\phi 10$ mm \times 20 mm and $\phi 10$ mm \times 40 mm are cored out from the cylindrical blocks using a water-cooled drilling machine at the speed of 480 rpm. However, the top and bottom surfaces of the cored specimens are not perfectly smooth due to operator error during the drilling. Therefore, every specimen is processed using a sanding machine and further polished (see Fig. 1).

The asphalt matrix is tested on a Dynamic Mechanical Analyzer instrument (NL-DMA-002) with a displacement precision of 0.001 mm, which is equipped with a thermal chamber to control the temperature. A loading cell with a

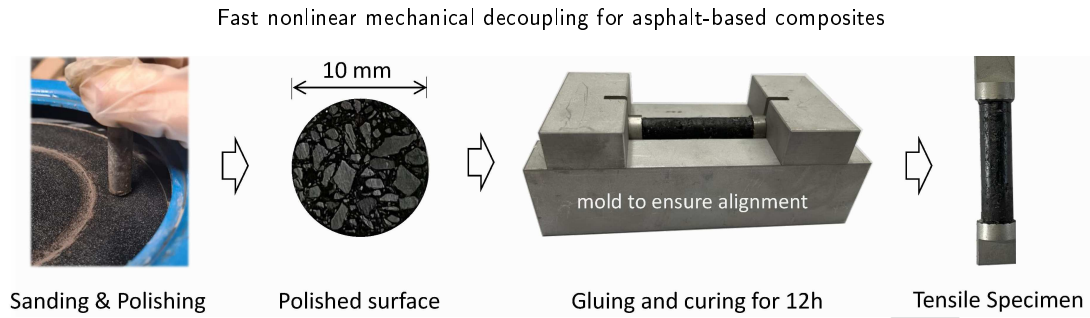


Figure 1: Specimen preparation: after coring the specimen from the big cylindrical block, both sides of every specimen need to be flattened and polished, in order to facilitate the gluing of the caps and the alignment required by the DMA machine.

maximum force of 500 N and accuracy of 0.1 N is mounted. As Fig. 2a shows, two disks are used for the compression test. For the test conducting the tensile load shown in Fig. 2b, a pair of clamps are specially designed to attach the sample to the machine. In the compression tests, a lubricant compatible with asphalt is added between the specimen and the steel disks to reduce the friction between the surfaces with the aim of minimizing the barreling effect, as is shown in Fig. 2a. For the tensile test, the specimen is too soft to be tightly clamped to the machine without causing deformation. Thus, a pair of aluminum caps are designed and glued to the two ends of the specimen using an epoxy resin with a curing time of 12 h, which allows the specimen to fit well in the clamps, as Fig. 1 and Fig. 2b illustrate. All the tests are conducted in the thermal chamber with a constant temperature of 24 ± 0.1 °C.

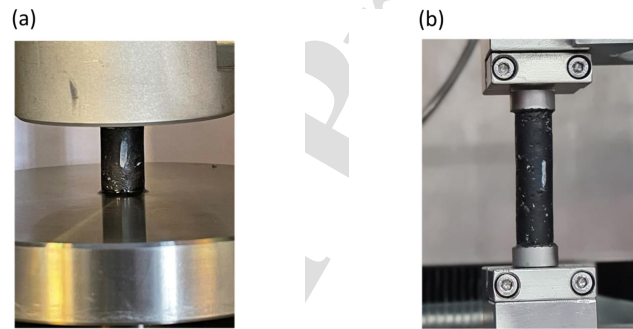


Figure 2: Experimental setups to determine the uniaxial response of the material: (a) short specimen designed for compression placed between the steel disks installed in the DMA machine; (b) long specimen designed for tension clamped to the DMA fixations.

3. Experimental campaign

A series of quasi-static tests under different strain rates are conducted to investigate the mechanical nonlinearities in the elastic, plastic, viscous and damage response of the asphalt matrix. These tests are further used to identify the key material properties to achieve the constitutive model. For each loading condition, 3 specimens are used to ensure the repeatability and reliability of the test results.

Due to the size limitations and material's nature, strain gauge and extensometer cannot be easily applied on the specimen. To obtain the true stress-strain response, full volume preservation hypothesis of the specimen is assumed. Therefore, the true stress and true strain can be expressed as $\sigma_{true} = (1 + \delta/L_0)F/A_0$ and $\epsilon_{true} = \ln(1 + \delta/L_0)$, respectively, where F is the applied force, A_0 is the original cross-section area, L_0 is the initial length of the specimen and δ is the displacement recorded by the machine sensor.

3.1. Rate-dependent monotonic loading

To better understand the rate-dependency of the material, five strain rates, 0.5, 1, 2, 3 and $5 (\times 10^{-3} \text{ s}^{-1})$, are chosen to conduct the uniaxial monotonic test in both compression and tension. The stress-strain behavior at different strain

Fast nonlinear mechanical decoupling for asphalt-based composites

rates is shown in Fig. 3.

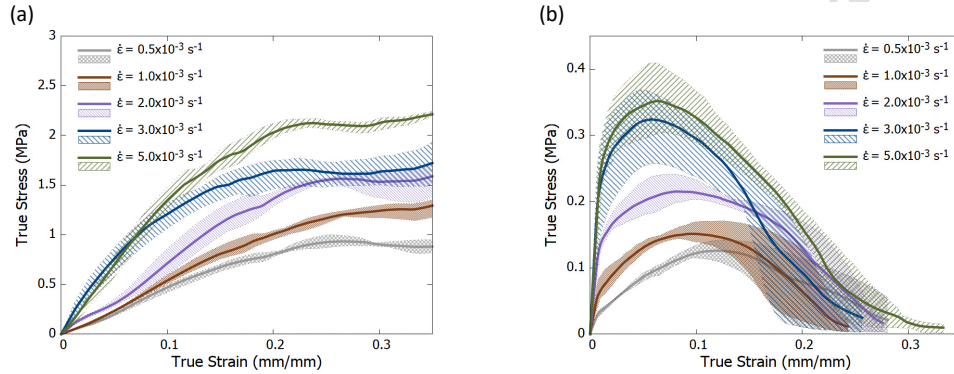


Figure 3: Rate-dependent stress-strain response of asphalt matrix under uniaxial monotonic loading: (a) compression; (b) tension. The solid curves and the shaded area represent the average result and the error band of each case, respectively.

Fig. 3 clearly shows the compression-tension (C-T) asymmetric behavior of the asphalt matrix under uniaxial monotonic loading. These results reveal that both the stiffness and strength of asphalt matrix are strongly rate-dependent within a narrow range of applied strain rate, varying more than 3 and 5 times in different loading directions, respectively. The softening curves in Fig. 3b indicate that the damage process is rate-dependent, and therefore, it should be considered in the constitutive model.

It should be noticed that compared to the tension test, the compression one involves additional technical difficulties coupled with intrinsic material uncertainties. For example, the contact between the specimen and the compression disks generates friction difficult to fully eliminate, although it was greatly reduced by adding lubricant as mentioned before. Some slight shape instabilities during loading due to misalignment of the deformed specimen were observed, likely caused by the lack of strict parallelism between the upper and the lower specimen surfaces. During the initial part of the loading, the specimen has to settle until these surfaces are in full contact with the compression disks. Although it could have been minimized by applying a slight pre-load on the specimen, the high compliance of asphalt can uncontrollably accelerate the plastic yielding. As a consequence, this settlement process might underestimate the initial stiffness, which explains the irregular tendency of the curve at the beginning of the load.

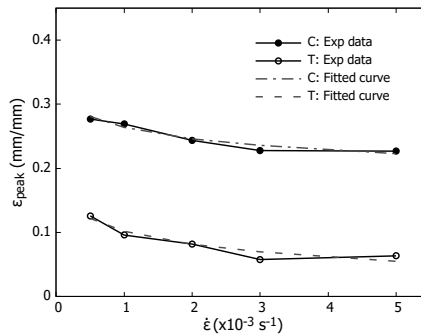


Figure 4: ϵ_{peak} at different strain rates in compression (C) and tension (T)

Fig. 4 shows the relationship between the strain (ϵ_{peak}) at the peak stress and the strain rate ($\dot{\epsilon}$) in compression (C) and tension (T), where, as a first approximation, a logarithm relationship can be proposed in the following way

Table 3

Fitted coefficients.

Coefficients	a	Ω	R^2
Compression	-0.025	0.98×10^4	0.9403
Tension	-0.029	1.11×10^7	0.9127

$$\epsilon_{\text{peak}} = a \ln \left(\Omega \frac{\dot{\epsilon}}{\dot{\epsilon}_s} \right) \quad (1)$$

where a is a material constant, $\dot{\epsilon}_s = c_s/l_{ele}$ is the propagation rate of stress waves in the material, $c_s = \sqrt{(\lambda + 2\mu)/\rho}$ is the wave speed, and l_{ele} is the characteristic length. The propagation rate of stress wave in asphalt matrix is calculated as $\dot{\epsilon}_s = 3.7 \times 10^5 \text{ s}^{-1}$. The proposed material constant Ω depends on the loading mode, which is further explained in the following paragraphs.

It should be noted that this first peak value is clear in case of tension, but less obvious in compression, where a process of apparent strain hardening takes place. By fitting Eq. 1 to the experimental curves, the coefficients a and Ω can be obtained, which are listed in Table 3. The determined function of ϵ_{peak} is further used in the rate-dependent damage initiation criterion in the following constitutive analysis of Sec.4.3.

The basic constituents of the asphalt matrix are the aggregates (agg) and the asphalt binder (bin), therefore assuming the Rule of Mixtures (ROM), Eq. 1 can be further extended to specify the C-T asymmetry:

$$\epsilon_{\text{peak}} = a \ln \left(\frac{\Omega^C \langle -\dot{\epsilon} \rangle + \Omega^T \langle \dot{\epsilon} \rangle}{\Phi \dot{\epsilon}_s^{\text{agg}} + (1 - \Phi) \dot{\epsilon}_s^{\text{bin}}} \dot{\epsilon} \right) \quad (2)$$

where the operator “ $\langle \cdot \rangle$ ” represents the Macaulay brackets defined as $\langle \dot{\epsilon} \rangle = (\dot{\epsilon} + |\dot{\epsilon}|)/2$ and Φ stands for the volume fraction of aggregates in the matrix. The characteristics strain rates given by $\dot{\epsilon}_s^{\text{agg}}$ and $\dot{\epsilon}_s^{\text{bin}}$ are proportional to the speed of stress wave in the aggregate and asphalt binder, respectively. It is important to notice that Eq. 2 applies the hypothesis of homogenization to the speed of stress waves, which is proportional to the elastic modulus.

In order to illustrate the consistency of Eq. 2, the analysis of the order of magnitude is conducted. Knowing the stiffness ($E^{\text{agg}} \approx 34 \text{ GPa}$, $E^{\text{bin}} \approx 10 \text{ kPa}$ at 24°C [68]), the volume fraction of aggregates ($\Phi = 0.896$) and the densities ($\rho^{\text{agg}} = 2700 \text{ kg/m}^3$, $\rho^{\text{bin}} = 1020 \text{ kg/m}^3$), the wave speed in each constituent yields $c_s^{\text{agg}} = 3.5 \times 10^6 \text{ mm/s}$ and $c_s^{\text{bin}} = 3.1 \times 10^3 \text{ mm/s}$, respectively. As a result, the follow relationship can be obtained:

$$\frac{\Omega^T}{\Omega^C} \approx \frac{\dot{\epsilon}_s^{\text{agg}}}{\dot{\epsilon}_s^{\text{bin}}} = \frac{c_s^{\text{agg}}}{c_s^{\text{bin}}} \approx 10^3 \quad (3)$$

where the ratio Ω_T/Ω_C indicates the proportional factor of stress wave speed in each material phase. It is worth mentioning that due to the high value of volume fraction of aggregates, during compression they tend to approach and come into contact, leading to the interlocking effect. This inter-aggregate interaction establishes a contact network in which the stress waves can travel more efficiently according to the speed of sound in the aggregates, which is exactly 3 order of magnitude larger than that in the binder. On the contrary, in case of tension, the aggregates tend to separate apart, therefore the stress waves are preferably transmitted through the soft asphalt binder [69, 70].

As Fig. 3a shows, when the material is compressed beyond around 30%, the softening curves start to increase due to the aforementioned interlocking process. This process occurs when the aggregates move slowly and start to touch each other when the specimen reaches a high level of internal compaction as it is schematically represented in Fig. 5 [71]. Under this situation, the mechanical contribution of the asphalt binder is negligible because, as mentioned, the load is essentially bear by the aggregates contact network. This can explain the visible stiffening effect observed in the stress-strain curves of Fig. 3a. The level of confinement in tension is much less than that in compression and the asphalt matrix fails earlier before the interlocking effect shows up.

The damage patterns of the tested specimens are shown in Fig. 6. Fig. 6a shows the specimen fully compacted

Fast nonlinear mechanical decoupling for asphalt-based composites

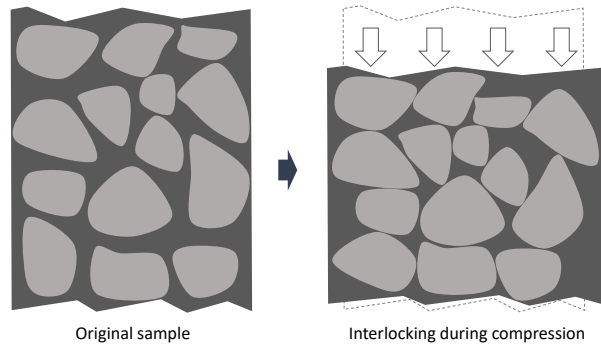


Figure 5: Schematic diagram of aggregate interlocking.

under compression. The cracks show up on the side surface of the specimen along the loading direction caused by the high circumferential tensile stresses, while there is no obvious crack in the center part. In the tension test, the micro-cracks and debonding firstly show up homogeneously distributed along the longitudinal axis of the specimen. When the micro-damage is accumulated to a certain degree, a visible macro-crack starts to initiate and propagate until total specimen breakage.

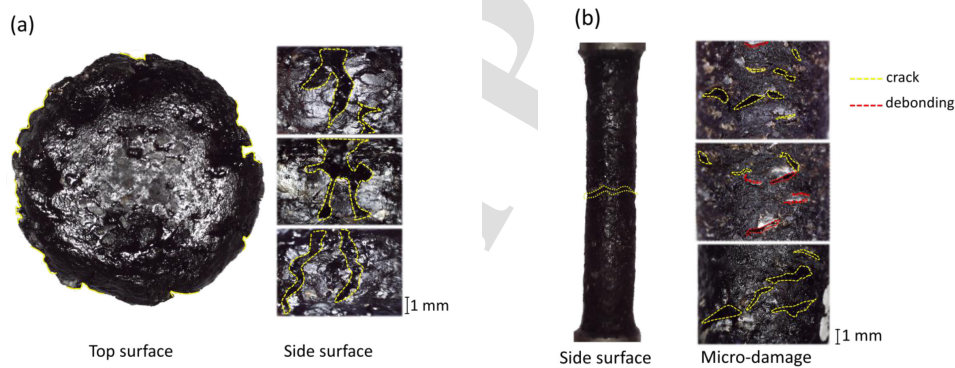


Figure 6: Damaged specimen after loading: (a) compression; (b) tension. The crack in the matrix and the debonding at the matrix-aggregate interface are highlighted in yellow and red, respectively.

To have a clearer overview of the damage evolution, an experimental observation of the degradation process of the specimen at two representative strain rates is represented in Fig. 7. First, the material homogeneously deforms during AB(A'B'). Then, microdamage starts to appear at the peak load, where Point B(B') indicates the initiation of damage. After that, more microcracks are observed on the specimen, which are homogeneously distributed along the loading direction as Point C(C') indicates. Stage BD(B'D') corresponds to the softening process during which the microcracks accumulates along the specimen. The difference between the curvature of the curves BD(B'D') and DE(D'E') indicates that a macro crack is formed and starts to propagate at Point D(D'), which leads to the final fracture afterward. By comparing the two strain rates cases, it can be found that the softening curve drops faster at the higher strain rate. Specifically, both the accumulation of microdamage and the propagation of macrocracks are faster at a higher strain rate, namely slope $BD > \text{slope } B'D'$ and slope $DE > \text{slope } D'E'$, which suggests that the damage in asphalt matrix is rate-dependent.

Fast nonlinear mechanical decoupling for asphalt-based composites

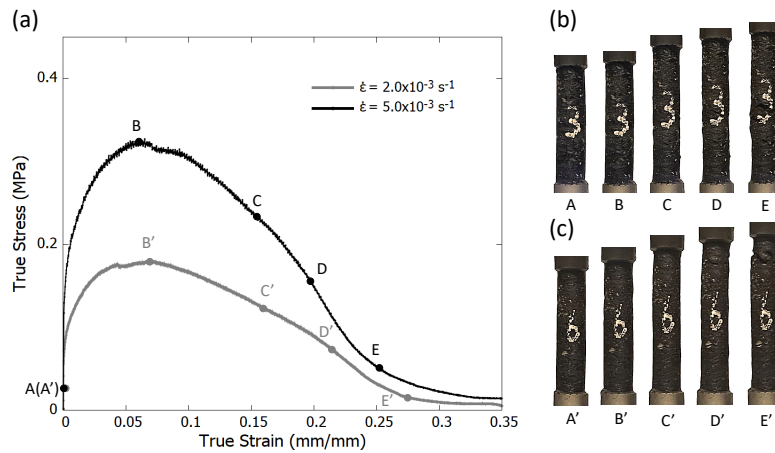


Figure 7: Damage evolution at different strain rates: (a) stress-strain curves; (b) snapshots of specimen degradation at $\dot{\epsilon} = 2 \times 10^{-3} \text{ s}^{-1}$; (c) snapshots of specimen degradation at $5 \times 10^{-3} \text{ s}^{-1}$.

3.2. Rate-dependent Loading-Unloading-Reloading

To better understand the viscous and plastic behaviors of asphalt matrix, cyclic Loading-Unloading-Reloading (LUR) test is conducted, where the permanent and recoverable strain can be quantified. It is important to clarify that these cycles are used to characterize inelastic strains, but not for assessing cyclic behavior with a high number of cycles under fatigue load. In each cycle, the specimen is firstly loaded at a constant strain rate to the aimed strain, unloaded at the same strain rate till zero force and then reloaded. Five strain rates, 0.5, 1, 2, 3 and 5 ($\times 10^{-3} \text{ s}^{-1}$), are chosen for both compression and tension. Typical results from the cyclic LUR test results are shown in Figure 8, on the right of which one LUR cycle is zoomed.

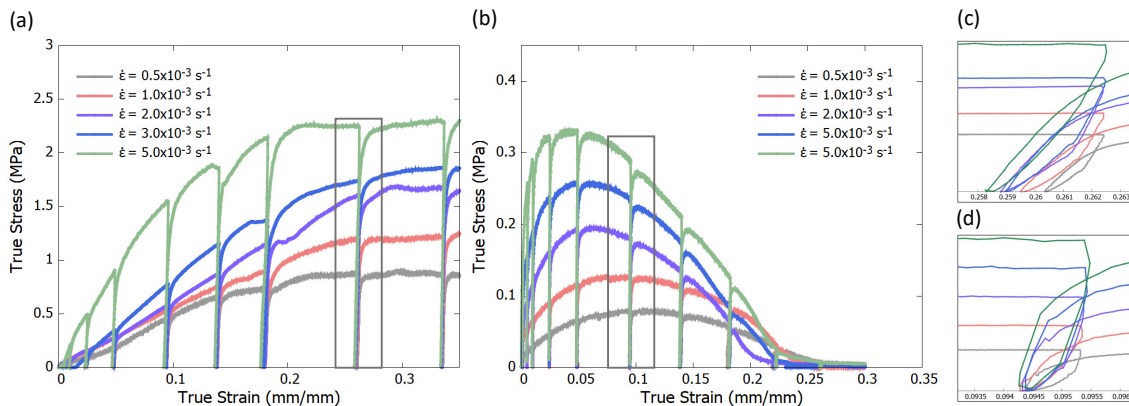


Figure 8: Stress-strain behavior in LUR tests at different strain rates: (a) compression; (b) tension; (c) zoomed LUR path in compression; (d) zoomed LUR path in tension.

The LUR test result illustrates that the material mainly shows viscoplastic behavior. As is shown in Fig. 9, the plastic strain is observed in the beginning of the loading, and it accumulates linearly with the increase of the total strain. Moreover, the plastic strain-total strain curves essentially overlap for different strain rates in both compression and tension.

The tensile LUR result is further used to extract more information on the damage evolution since it covers the whole degradation process of the material until the final failure. To do this, the procedure explained in Appendix A has been developed to compute objectively and systematically the magnitude of the material stiffness degradation

Fast nonlinear mechanical decoupling for asphalt-based composites

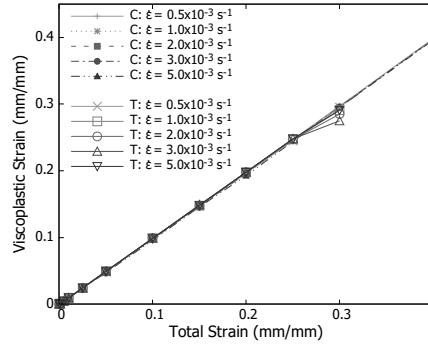


Figure 9: Relationship between viscoplastic strain and total strain at different strain rates in compression (C) and tension (T).

during the unloading and reloading process. This procedure detects the number of LUR events in every stress-strain curve corresponding to all tested strain rates. Every LUR loop is determined by detecting the self-intersection present in the curve. Two numbers are obtained from each loop: the secant slope and the enclosed area. The secant represents the average stiffness in such a loop, which provides a direct measure of the material stiffness after reaching certain level of damage. Fig. 10 shows that the unloading slope decreases as the accumulation of the plastic strain increases, revealing the evolution of damage. The difference among the decreasing curves at different strain rates indicates that the damage evolution is rate dependent.

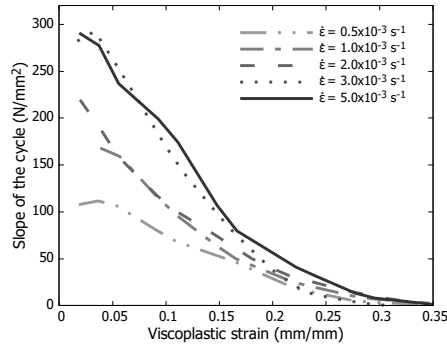


Figure 10: Evolution of the stiffness degradation as a function of the viscoplastic strain at different strain rates from the tensile LUR test. This stiffness is obtained from the unloading path using the algorithm described in Appendix A.

4. Constitutive material model

An elasto-viscoplastic-viscodamage (E-VP-VD) model is proposed to describe the mechanical behavior of asphalt matrix based on the experimental observations. This section introduces first the basic definitions in the finite strain kinematic formulation, which is suitable to describe large deformations due to material's flow and it is very convenient to incorporate rate effects. After that, the components of the model, namely, elasto-viscoplastic and visco-damage are described.

4.1. Finite strain kinematic framework and thermodynamics in brief

The material model based on the kinematic formulation rely on the fact that the total deformation gradient can be multiplicatively decomposed into elastic and inelastic parts [72] as follows:

$$\mathbf{F} = \mathbf{F}_e \mathbf{F}_i \quad (4)$$

where the subscript e and i denote the elastic and inelastic part, respectively.

The total deformation gradient \mathbf{F} is related to the rate of the deformation gradient $\dot{\mathbf{F}}$ via the velocity gradient \mathbf{L} given by

$$\mathbf{L} = \dot{\mathbf{F}}\mathbf{F}^{-1} = \dot{\mathbf{F}}_e \mathbf{F}_e^{-1} + \mathbf{F}_e \mathbf{L}_i \mathbf{F}_e^{-1} \quad (5)$$

where \mathbf{L}_i is the inelastic velocity gradient expressed in the relaxed configuration. Thus, if the elastic stresses are released, the body will retain only the inelastic contribution, therefore this inelastic velocity gradient can be written as

$$\mathbf{L}_i = \dot{\mathbf{F}}_i \mathbf{F}_i^{-1} = \mathbf{D}_i + \mathbf{W}_i \quad (6)$$

where \mathbf{W}_i is the inelastic spin tensor. Considering an isotropic material, it leads to a spin-free inelastic velocity gradient that permits to assume that $\mathbf{W}_i = 0$ [73]. Therefore, the time derivative of the inelastic deformation gradient is finally given by

$$\dot{\mathbf{F}}_i = \mathbf{D}_i \mathbf{F}_i \quad (7)$$

To approximately preserve the inelastic incompressibility condition, the midpoint scheme is adopted [74, 75], where the inelastic evolution can be integrated as follows

$$\begin{aligned} \mathbf{F}_i(t + \Delta t) &= \mathbf{F}_i(t) + k_2 \Delta t \\ k_1 &= \dot{\mathbf{F}}_i(t, \mathbf{F}_i(t)) \\ k_2 &= \dot{\mathbf{F}}_i\left(t + \frac{1}{2}\Delta t, \mathbf{F}_i(t) + \frac{1}{2}k_1 \Delta t\right) \end{aligned} \quad (8)$$

Then, the elastic deformation gradient is updated from

$$\mathbf{F}_e = \mathbf{F} \mathbf{F}_i^{-1} \quad (9)$$

The rate of inelastic deformation is expressed as

$$\mathbf{D}_i = \dot{\epsilon} \mathbf{N} \quad (10)$$

where $\dot{\epsilon}$ represents the prescribed inelastic equivalent strain rate. Depending on the constitutive model, $\dot{\epsilon}$ can be function of shear stress, hydrostatic pressure, temperature, crystallization or humidity. The 2nd order tensor \mathbf{N} provides the direction of the driving stress indicating the direction where the inelastic deformation yields and evolves over time [76]. This direction tensor is defined in this work as follows

$$\mathbf{N} = \frac{\partial \phi}{\partial \boldsymbol{\sigma}} \quad (11)$$

As an example, in case of assuming a Von Mises yield function and associated plastic flow, this direction tensor can be written as follows

$$\mathbf{N} = \frac{1}{\sqrt{2}} \frac{\boldsymbol{\sigma}'}{\tau} \quad (12)$$

Fast nonlinear mechanical decoupling for asphalt-based composites

where σ' is the deviatoric stress tensor defined as

$$\sigma' = \sigma - \frac{1}{3}\text{tr}[\sigma]\mathbf{I} \quad (13)$$

being σ the stress tensor and τ the equivalent shear stress expressed as

$$\tau = \sqrt{\frac{1}{2}\sigma' : \sigma'} \quad (14)$$

In these expressions, the symbol $\text{tr}[\]$ represent the trace operation, \mathbf{I} is the 2nd order identity tensor and “:” operator stands for the scalar product of 2nd order tensors, also referred as the double contraction or double inner product which is given by $\mathbf{X} : \mathbf{Y} = X_{ij}Y_{ij}$ with \mathbf{X} and \mathbf{Y} two generic 2nd order tensors with indices i and j along the Cartesian coordinate axes.

This paper studies the mechanical response at room temperature, therefore from the thermodynamic point of view, the Clausius-Duhem inequality for an isothermal process is given as follows

$$\sigma : \mathbf{L} - \dot{\psi} \geq 0 \quad (15)$$

where $\dot{\psi}$ is the time derivative of the Helmholtz free energy density. In the context of irreversible thermodynamics, the constitutive equations and the evolutions laws of the variables can be obtained from Helmholtz energy which can be formally expressed as

$$\psi = \psi(\mathbf{h}_e, d, q) = \psi_e(\mathbf{h}_e, d) + \psi_p(q) \quad (16)$$

where d is an internal damage variable and q is a strain-like internal variable whose time derivative is related to the inelastic rate of deformation expressed by Eq. 10. The elastic Hencky strain tensor $\mathbf{h}_e = \ln\sqrt{\mathbf{B}_e}$ is calculated using the left Cauchy Green deformation tensor $\mathbf{B}_e = \mathbf{F}_e \mathbf{F}_e^T$ (i.e., $B_{e,ij} = F_{e,ik} F_{e,jk}$). It can be noticed that Eq. 16 has been partitioned into elastic and plastic components by assuming the hypothesis of decoupling between the elastic-damage and plastic responses. The first part assumes that a growing damage will lead to release the elastic strain energy, whilst the second part accounts for the plastic dissipation. After decomposing the strain into elastic and plastic parts and by defining the variable $\zeta = \partial\psi_p/\partial q$, the reduced internal dissipation can be written as

$$\sigma : \dot{\mathbf{h}}_p - \zeta \dot{q} + Y_d \dot{d} \geq 0 \quad (17)$$

where Y_p is the thermodynamic force associated with the damage process which is defined as $Y_d = -\partial\psi_e/\partial d$. To ensure fully decoupling, this work assumes that plastic flow can take place without damage, and similarly, any damage event can happen without appreciable plastic flow. As a consequence, the second principle of thermodynamics under these conditions can be expressed separately as

$$\sigma : \dot{\mathbf{h}}_p - \zeta \dot{q} \geq 0 \quad Y_d \dot{d} \geq 0 \quad (18)$$

Postulating the shape of Eq. 16 and imposing a constrain to the yield function ϕ via the Lagrange multiplier Λ , the flow rule and evolution of the plastic strain and strain-like variable are obtained according to the principle of minimum energy dissipation, namely

$$\frac{\partial \Pi}{\partial \sigma} = 0 \quad \frac{\partial \Pi}{\partial \zeta} = 0 \quad \text{with} \quad \Pi = \sigma : \dot{\mathbf{h}}_p - \zeta \dot{q} - \Lambda \phi \quad (19)$$

In rate-independent plasticity theory, the plastic multiplier Λ is not material function and, after solving the optimization problem of Eq. 19 it provides the plastic strain rate tensor and equivalent plastic strain rate, respectively, as it follows

$$\mathbf{h}_p = \Lambda \frac{\partial \phi}{\partial \sigma} \quad \dot{q} = \Lambda \frac{\partial \phi}{\partial \zeta} \quad (20)$$

However, in rate-dependent plasticity, the quantity Λ can be prescribed by defining a constitutive model. A similar

treatment holds for the damage-related part. In that sense, this paper makes use of the Eq. 10 to equivalently impose such as constitutive model, as it will presented in the next section. Nevertheless, by prescribing directly the rate form of the viscoplastic multiplier does not prevent to find the corresponding rate-dependent yield function ϕ .

4.2. Elasto-ViscoPlastic component

To precisely describe the nonlinear behavior of the asphalt matrix prior to any damage event, an elasto-viscoplastic (E-VP) model is proposed first. This part of the model is represented in a rheological form in Fig. 11 consisting of a nonlinear dashpot and a linear spring connected in series. The nonlinear dashpot model provides a viscous component enabling to incorporate rate-dependency and relaxation behavior of materials experiencing creep effects.

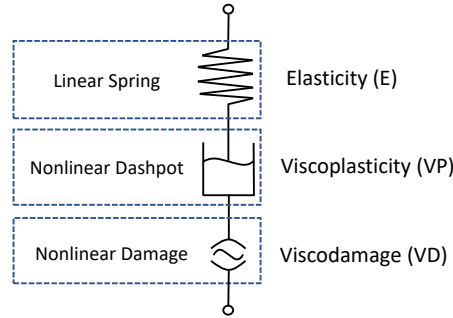


Figure 11: Schematic representation of the E-VP-VD constitutive model, consisting of three rheological elements connected in series.

In this work, this component is formulated using as a base the constitutive model devised by Bergström and Boyce (BB) [77]. Their initial model was formulated to describe the rate- and time-dependent behavior of highly dissipative materials and it consisted in a dashpot connected to two hyperelastic springs in order to reproduce the response of some elastomers like neoprene. This model can be physically comprehended by resorting on the micromechanics of the macromolecular polymer network deformation. In that case, the material could be seen as a network with long molecular chains and superimposed entanglements consisting of free molecular chains. Apart from the deformation of the cross-linking network, the free chains contribute with additional deformation. The dangling chain ends start to move combining Brownian and reptational motions during continuous stretching, which causes the creep-like effect.

However, to represent ABC in this research, the proposed model makes use only of the viscous component of the BB model. Based on the experimental observations, this component permits to describe the viscous-based inelastic mechanism in pure asphalt matrix because it can capture well the inelastic response when it is connected to a linear elastic element.

The original viscoplastic strain increment deduced by Bergström and Boyce is devoid of the mechanical response due to pressure. However, this is a crucial feature in ABC materials to explain the Compression-Tension (C-T) asymmetry [11, 78]. Therefore, the modified expression captures the tension-compression asymmetry by incorporating a pressure-dependent term. It is given by

$$\dot{\epsilon}_B = C_1 (\lambda_{\text{chain}} - 1)^{C_2} \left| \frac{\tau - \xi P}{\tau_B} \right|^m \quad (21)$$

where the constant C_1 is a reference effective creep rate and C_2 controls the kinetics of relaxation ($C_2 \leq 0$). The tension-compression asymmetry is controlled by the hydrostatic pressure $P = -\frac{1}{3}\text{tr}[\sigma]$ term by a pressure sensitivity coefficient ξ . The coefficient ξ is a function of the ratio between plastic yield stresses in tension and compression and is also considered a material parameter. The ratio $|(\tau - \xi P)/\tau_B|^m$ indicates the stress dependency on the energy-activated creep behavior, where m controls the inelastic flow and τ_B is considered as a material constant. The coefficient ξ is a function of the ratio between plastic yield in compression and tension. The specific shape of this function is under current research and it is left out of the scope of this paper. The sensitivity analysis of the parameters C_1, C_2, m, τ_B is

summarized in Appendix B, which illustrates the rate-dependency and their effects on the general behavior, e.g., the curve curvature, the slope of unloading path, permanent strain or hysteresis effects.

In Eq. 21, the inelastic network stretch λ_{chain} is obtained as the principal macroscopic stretch state from the eight-chain model by Arruda and Boyce [79]. It is expressed in terms of left Cauchy-Green strain tensor $\mathbf{B}_i = \mathbf{F}_i \mathbf{F}_i^T$ ($B_{i,ij} = F_{i,ik} F_{i,kj}$), given by

$$\lambda_{\text{chain}} = \sqrt{\frac{1}{3} \text{tr} [\mathbf{B}_i]} \quad (22)$$

Beside the deviatoric part governed by equivalent shear stress τ defined in Eq. 14.

This viscous element is connected in series with a linear elastic spring providing the following elastic stress tensor

$$\boldsymbol{\sigma}_e = \frac{1}{\det[\mathbf{F}_e]} (\lambda \text{tr}[\mathbf{h}_e] \mathbf{I} + 2\mu \mathbf{h}_e) \quad (23)$$

where λ and μ are the Lamé coefficients. At this step of the calculation, the elastic part of the deformation gradient \mathbf{F}_e is obtained from Eq. 9, or in other words, the elastic stress is obtained after updating \mathbf{F}_i (Eq. 8) as a result of inserting Eq. 21 in Eq. 10, namely, setting $\dot{\boldsymbol{\varepsilon}} = \dot{\boldsymbol{\varepsilon}}_B$.

It should be noted that in case of implicit calculation, the consistent tangent modulus is required, which is derived as follows.

In the continuum framework, the effective stress in an elastic-viscoplastic system is computed using the elastic strain, which is obtained by eliminating the viscoplastic part from the total strain increment ($\Delta \boldsymbol{\varepsilon}_e = \Delta \boldsymbol{\varepsilon} - \Delta \boldsymbol{\varepsilon}_i$). At any instance of the time-step $t + \Delta t$, the stress is computed as

$$\boldsymbol{\sigma}_e(t + \Delta t) = \boldsymbol{\sigma}_e(t) + \mathbb{C}_e : \Delta \boldsymbol{\varepsilon}_e = (\boldsymbol{\sigma}_e(t) + \mathbb{C}_e : \Delta \boldsymbol{\varepsilon}) - \mathbb{C}_e : \Delta \boldsymbol{\varepsilon}_i. \quad (24)$$

From the above equation, $\boldsymbol{\sigma}_e(t) + \mathbb{C}_e : \Delta \boldsymbol{\varepsilon}$ constitutes to the predicted (trial) stress $\boldsymbol{\sigma}^{tr}$, and therefore it can be rewritten as

$$\boldsymbol{\sigma}_e(t + \Delta t) = \boldsymbol{\sigma}^{tr} - \mathbb{C}_e : \Delta \boldsymbol{\varepsilon}_i. \quad (25)$$

The elimination process of the viscoplastic part in the above stress relation (Eq. 24) is representative of the implicit elastic predictor method. The implicit elastic predictor (radial return mapping) method is a conventional approach to map the excessively predicted stress along the normal to the yield surface and the magnitude of inelastic strain increment (Eq. 21). The inelastic strain increment is, therefore expressed as

$$\Delta \boldsymbol{\varepsilon}_i = \Delta \bar{\boldsymbol{\varepsilon}}_B \mathbf{N} = (\dot{\boldsymbol{\varepsilon}}_B \Delta t) \mathbf{N}. \quad (26)$$

Using the potential function $g(\tau, \sigma_y) = \sqrt{2}\tau - \tau_y$ similar to von Mises yield theory and based on τ and arbitrary yield stress in shear τ_y whose value is dependent on the mode of loading, the yield surface normal tensor following non-associated flow rule can be derived as

$$\mathbf{N} = \frac{\partial g}{\partial \boldsymbol{\sigma}} = \frac{1}{\sqrt{2}} \frac{\boldsymbol{\sigma}'}{\tau}. \quad (27)$$

The consistent elastic-viscoplastic tangent modulus is derived using the stress update equation (Eq. 25) by considering the trial stress as elastic. It is given by

$$\mathbb{C}_{ep} = \mathbb{C}_e - 2\mu \Delta \bar{\boldsymbol{\varepsilon}}_B \frac{\partial \mathbf{N}}{\partial \boldsymbol{\varepsilon}} - (\mathbb{C}_e : \mathbf{N}) \otimes \frac{\partial \Delta \bar{\boldsymbol{\varepsilon}}_B}{\partial \boldsymbol{\varepsilon}}. \quad (28)$$

Individual terms of tangent modulus (Eq. 28) require rigorous tensorial calculus derivation processes and thus

Fast nonlinear mechanical decoupling for asphalt-based composites

shall be expanded individually. The elastic jacobian \mathbb{C}_e is expressed as

$$\mathbb{C}_e = \frac{\partial \boldsymbol{\sigma}'^r}{\partial \boldsymbol{\varepsilon}} = 2\mu \mathbb{P} + \kappa \bar{\mathbb{I}} \quad (29)$$

where the 4th order tensors: $\mathbb{P} = \mathbb{I} - \frac{1}{3}\bar{\mathbb{I}}$ is the projection tensor (or deviatoric operator), $\bar{\mathbb{I}} = \mathbf{I} \otimes \mathbf{I}$ is the hydrostatic operator and $\mathbb{I} = (\mathbf{I} \otimes \mathbf{I})^{\mathbb{T}}$ is the identity tensor. They respectively cause to reduce an arbitrary tensor of 2nd order \mathbf{A} upon double contraction to its deviatoric form $\mathbb{P} : \mathbf{A} = \mathbf{A}'$, hydrostatic form $\bar{\mathbb{I}} : \mathbf{A} = \text{tr}[\mathbf{A}]\mathbf{I}$ and its original form $\mathbb{I} : \mathbf{A} = \mathbf{A}$.

In the second term, the partial derivative of the surface normal \mathbf{N} with respect to strain tensor $\boldsymbol{\varepsilon}$ is a 4th order tensor, derived as

$$\frac{\partial \mathbf{N}}{\partial \boldsymbol{\varepsilon}} = \frac{2\mu}{\sqrt{2\tau}} (\mathbb{P} - \mathbf{N} \otimes \mathbf{N}) \quad (30)$$

where μ is the shear modulus.

The last term includes a partial differentiation of equivalent inelastic strain increment $\Delta \bar{\boldsymbol{\varepsilon}}_B$ with respect to strain tensor. It yields a 2nd order tensor given by

$$\frac{\partial \Delta \bar{\boldsymbol{\varepsilon}}_B}{\partial \boldsymbol{\varepsilon}} = \Delta \bar{\boldsymbol{\varepsilon}}_B \left(\frac{C_2}{\lambda_{\text{chain}} - 1} \frac{\partial \lambda_{\text{chain}}}{\partial \boldsymbol{\varepsilon}} + \frac{m}{|\tau - \xi P|} \frac{\partial |\tau - \xi P|}{\partial \boldsymbol{\varepsilon}} \right). \quad (31)$$

Each of the terms containing partial differentiations from Eq. 31 can be further expanded as

$$\frac{\partial \lambda_{\text{chain}}}{\partial \boldsymbol{\varepsilon}} = \left(\frac{\partial \boldsymbol{\varepsilon}}{\partial \mathbf{F}} \right)^{-1} : \frac{\partial \lambda_{\text{chain}}}{\partial \mathbf{F}} = \left\{ \frac{1}{2} (\mathbb{I}^{\mathbb{T}} \mathbf{F} + \mathbf{F}^{\mathbb{T}} \mathbb{I}) \right\}^{-1} : \frac{1}{3} \frac{\mathbf{F}}{\lambda_{\text{chain}}}. \quad (32)$$

$$\frac{\partial |\tau - \xi P|}{\partial \boldsymbol{\varepsilon}} = \mu \frac{\boldsymbol{\sigma}'}{\tau} + \kappa \xi \mathbf{I} \quad (33)$$

where $\mathbb{I}^{\mathbb{T}} = (\mathbf{I} \otimes \mathbf{I})^{\mathbb{T}}$ in Eq. 32 is a transpose operator causing transpose of a 2nd order tensor upon double contraction, $\mathbb{I}^{\mathbb{T}} : \mathbf{A} = \mathbf{A}^{\mathbb{T}}$. However, the 4th order tensor $(\mathbb{I}^{\mathbb{T}} \mathbf{F} + \mathbf{F}^{\mathbb{T}} \mathbb{I})$ is non-invertible due to singularity (i.e., $\det[\mathbb{I}^{\mathbb{T}} \mathbf{F} + \mathbf{F}^{\mathbb{T}} \mathbb{I}] = 0$) and shall be ignored.

The consistent elastic-viscoplastic tangent modulus in Eq. 28 can be collectively reordered as

$$\mathbb{C}_{ep} = (2\mu \mathbb{P} + \kappa \bar{\mathbb{I}}) - \left[\frac{4\mu^2}{\sqrt{2\tau}} (\mathbb{P} - \mathbf{N} \otimes \mathbf{N}) - (\mathbb{C}_e : \mathbf{N}) \otimes \frac{m}{|\tau - \xi P|} \left(\mu \frac{\boldsymbol{\sigma}'}{\tau} + \kappa \xi \mathbf{I} \right) \right] \Delta \bar{\boldsymbol{\varepsilon}}_B. \quad (34)$$

4.3. ViscoDamage component

A viscodamage (VD) model is proposed to capture the rate-dependent softening behavior of asphalt matrix, which is schematically represented in the lowest block of Figure 11. The damage process generally affects the elastic properties and the plastic deformation as they are inherently coupled. However, the present damage approach consists in a two-steps process (initiation and further propagation) affecting the resulting elastic stress of the E-VP part by means of direct isotropic degradation process. Here it is assumed that smeared cracks and voids are homogeneously and equally distributed in the sample along all directions. This fact has been experimentally observed in the current samples between points B and C from Fig. 7. Small defects grow creating irregular but randomly oriented voids that finally trend to coalescence in multiple directions (no a clear crack plane is observed).

4.3.1. Damage initiation criterion

Based on the experimental results, the strain-based criterion is chosen to determine the damage initiation timing. That is to say, damage initiates when the principal value of the current strain is larger than the experimentally determined strain at loading peak ($\varepsilon_{\text{peak}}$). This means that the initiation of damage depends on the different level of strain

at different loading rate. As it is mentioned in Section 3.1, ϵ_{peak} is determined as a function of $\dot{\epsilon}_{\text{peak}}$ in Eq. 1, which has been implemented in the VD model as the rate-dependent damage initiation criterion. This is a practical approach as it is relatively straightforward to determine the peak stress from the proposed testing procedure.

4.3.2. Rate-dependent damage evolution law

The rate-dependent damage rate evolution law is defined in this work as

$$\dot{d} = \dot{d}_{\infty} \left(1 - e^{-\frac{\dot{\epsilon}_{\text{eff}}}{\dot{\epsilon}_s} \eta} \right) \quad (35)$$

where $\dot{\epsilon}_{\text{eff}} = \sqrt{\frac{2}{3} \dot{\mathbf{h}} : \dot{\mathbf{h}}}$ is the effective strain rate, $\dot{\mathbf{h}}$ is the calculated Hecky-based strain rate tensor, $\dot{\epsilon}_s$ is the propagation rate of stress waves (see Section 3.1), η is a dimensionless damping coefficient which is a material constant controlling the ratio between the effective strain rate and intrinsic material strain rate, and \dot{d}_{∞} is the damage evolution rate at $\dot{\epsilon}_{\text{eff}} = \infty$, which indicates the fastest damage propagation process.

To better understand the effect of each damage parameter, a sensitivity analysis of \dot{d}_{∞} and η is conducted at the strain rate of 0.5×10^{-3} . Here, $\dot{d}_{\infty} = 10^6 \text{ s}^{-1}$ and $\eta = 2.064$ are used as the reference values, which are obtained from the optimization process explained in Section 5.4. The propagation rate of stress wave in asphalt matrix $\dot{\epsilon}_s = 3.7 \times 10^5 \text{ s}^{-1}$ is calculated and used in this sensitivity analysis. As Fig. 12a shows, the increase of \dot{d}_{∞} can cause a decrease in the damage rate. The optimal \dot{d}_{∞} is one order of magnitude larger than $\dot{\epsilon}_s$. When $\dot{d}_{\infty} \gg \dot{\epsilon}_s$, the material shows a pure brittle behavior since a sudden fracture is observed after damage initiation. When $\dot{d}_{\infty} \ll \dot{\epsilon}_s$ there is barely damage effect observed as the softening and the undamaged curves almost overlap. Fig. 12b illustrates that η has the opposite effect on the damage rate. When $\eta > 50$, namely $\frac{\dot{\epsilon}_{\text{eff}}}{\dot{\epsilon}_s} \eta > 10^2$, the material shows pure brittle behavior. When $\eta < 0.01$, namely $\frac{\dot{\epsilon}_{\text{eff}}}{\dot{\epsilon}_s} \eta < 10^{-1}$, the material almost produces a non-damage response.

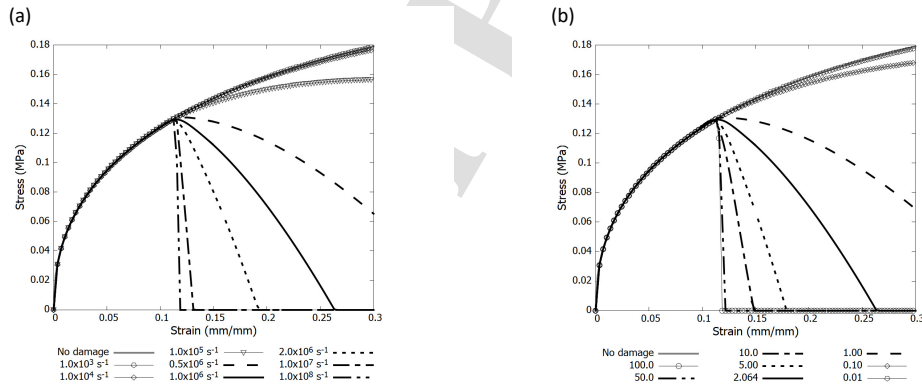


Figure 12: Sensitivity analysis of the damage parameters: (a) effect of \dot{d}_{∞} ($\eta=2.064$); (b) effect of η ($\dot{d}_{\infty}=1.0 \times 10^6$).

At every time increment Δt , the evolution of the damage variable is explicitly integrated over the time using Eq. 35. The updated damage variable $d(t + \Delta t)$ is employed to degrade the resulting stress tensor generated by the E-VP component by making use of the effective stress concept proposed by Kachanov [80].

A fully coupled description of the model involves damage affecting both the elastic and the viscoplastic regions. The cyclic LUR test was designed to quantify the variations of stiffness. Based on the experimental observations, no stiffness degradation was found before the peak stress after performing LUR tests. The specimens only produced some permanent strain without quantifiable change in the slope of the unloading-reloading path. Therefore, it is assumed that damage is mainly initiated after reaching the peak stress thus essentially affecting the viscoplastic part. It is worth noting that this assumption might oversimplify the true effect of damage on the whole loading history. But it is also true that, before the peak stress, damage is entangled with the plastic yielding, being the latter much more dominant in the material at that loading moment.

Following this hypothesis, the proposed model applies the degradation factor $(1-d)$ on the overall response, which

is equivalent to mapping the pristine E-VP part to the softening curve according to the damage evolution in Eq. 35. To do this, the elasto-viscoplastic stress is transformed as

$$\boldsymbol{\sigma} = \mathbf{Q}(\text{diag}[\boldsymbol{\sigma}_e](1 - d))\mathbf{Q}^T \quad (36)$$

where \mathbf{Q} is the eigen-decomposition transformation matrix for 2nd order tensor. It should be noted that the tangent modulus is needed in case of implicit calculations since Abaqus/Standard requires this tensor to internally solve the equation system via Newton-Raphson method. Thus, the consistent tangent modulus considering damage is given by

$$\mathbb{C} = \mathbf{Q}(\text{diag}[\mathbb{C}_{ep}](1 - d))\mathbf{Q}^T \quad (37)$$

where \mathbf{Q} is the eigen-decomposition transformation matrix for 4th order tensor. The practical implementation is shown in the following.

4.4. Numerical implementation

Algorithm 1 presents the general functioning of the proposed E-VP-VD model. This scheme can be straightforwardly implemented as a user-defined subroutine (V)UMAT for the solvers available in the Finite Element software Abaqus [64]. The algorithm consists of three basic stages, (i) in lines 1-4, the stress, strain increment and total deformation gradients are retrieved from previous time increment, as well as the deformation gradient for the current instant, (ii) lines 5-11 are used to update the inelastic part of the deformation gradient of the viscoplastic element and its associated stress and consistent tangent modulus, and (iii) lines 12-21 are used to evaluate if the damage initiation condition is met, in which case, the damage variable is updated and applied to the previous stress tensor. It is worth noting that in case of using an implicit solver (UMAT), lines 11, 18 and 21 must be provided.

5. Multi-constrain-based material parameter identification

This section describes the material parameters identification (MPI) procedure that allows for determining the constitutive material constants using the experimental results under different loading conditions simultaneously. An in-house improved multidimensional Nelder-Mead gradient-less algorithm is developed and integrated in the FEM framework for the MPI. The proposed approach is designed to incorporate multiple user-defined and physical-based constraints leading to approach highly non-linear functions in an efficient way.

5.1. Modified Nelder-Mead optimization

As one of the gradient-less downhill simplex methods, Nelder-Mead (N-M) algorithm is commonly adopted for nonlinear optimization in material parameter identification [81–83]. The original N-M method is based on the iterative update of an n -dimensional analogue figure of triangles consisting of $n+1$ points in an n -dimensional space [84]:

$$\{\mathbf{x}_i\} = [\mathbf{x}_1 \quad \mathbf{x}_2 \quad \dots \quad \mathbf{x}_{n+1}] \quad (38)$$

where each point is an array \mathbf{x}_i consisting of n parameters to be identified:

$$\mathbf{x}_i = \begin{bmatrix} x_i^{(1)} \\ x_i^{(2)} \\ \dots \\ x_i^{(n)} \end{bmatrix} \quad (39)$$

During the optimization, each point is updated following a set of operations and the old one is replaced with a better point to minimize the objective function $f(\mathbf{x})$. Fig. 13 shows the geometric operations in the N-M method, which are visualized as a set of tentative movements on top of a complex surface, aiming at finding the local minimum. The test points are firstly ordered as:

$$f(\mathbf{x}_1) \leq f(\mathbf{x}_2) \leq \dots \leq f(\mathbf{x}_{n+1}) \quad (40)$$

Algorithm 1: Stress update integration scheme

```

▶ Get stress and deformation tensors:
1    $\sigma_e(t) \leftarrow$  stress tensor at  $t$ 
2    $\Delta\varepsilon \leftarrow$  strain increment at  $t$ 
3    $F(t) \leftarrow$  deformation gradient tensor at the beginning of the step
4    $F(t + \Delta t) \leftarrow$  deformation gradient tensor at the end of the step
▶ Calculation of the non-linear dashpot:
5   ▷ Compute:  $\lambda_{\text{chain}} \leftarrow$  Eq. 22
6   ▷ Compute:  $\dot{\varepsilon} \leftarrow$  Eq. 21
7   ▷ Compute:  $\dot{F}_i \leftarrow$  Eq. 7
8   ▷ Compute:  $F_i(t + \Delta t) \leftarrow$  Eq. 8
   /* Integrating Eq. 7 over time using explicit midpoint integration scheme*/
▶ Elastic stress calculation:
   ▷ Update elastic deformation gradient:
9    $F_e(t + \Delta t) \leftarrow$  Eq. 9
   ▷ Update elastic stress tensor:
10   $\sigma_e^{tr}(t + \Delta t) \leftarrow$  Eq. 23
▶ Consistent tangent modulus calculation: /*Implicit*/
11   $C_{ep}^{tr}(t + \Delta t) \leftarrow$  Eq. 34
▶ Strain-based damage initiation criterion:
12   $\varepsilon_{\text{peak}} \leftarrow$  Eq. 1
▶ Determine damage initiation and evolution:
13  if  $\varepsilon > \varepsilon_{\text{peak}}$  and  $\Delta\varepsilon > 0$  and  $\Delta\sigma < 0$  then
14  |   ▷ Compute:  $\dot{\varepsilon}_{\text{eff}}$ 
15  |   ▷ Compute:  $d \leftarrow$  Eq. 35
16  |   ▷ Compute:  $d+ = d\Delta t$ 
17  |   ▷ Result:
18  |    $\sigma(t + \Delta t) \leftarrow$  Eq. 36
19  |    $C(t + \Delta t) \leftarrow$  Eq. 37 /*Implicit*/
20  else
21  |   ▷ Result:
22  |    $\sigma(t + \Delta t) \leftarrow \sigma_e^{tr}(t + \Delta t)$ 
23  |    $C(t + \Delta t) \leftarrow C_{ep}^{tr}(t + \Delta t)$  /*Implicit*/
24  end
25  return

```

where \mathbf{x}_1 and \mathbf{x}_{n+1} indicate the best and worst points, respectively. Then, \mathbf{x}_0 is calculated as the centroid point of all points except \mathbf{x}_{n+1} . The reflection \mathbf{x}_r of the current worst point \mathbf{x}_{n+1} is given by

$$\mathbf{x}_r = \mathbf{x}_0 + \alpha(\mathbf{x}_0 - \mathbf{x}_{n+1}) \quad (\alpha > 0) \quad (41)$$

where α is the reflection coefficient and it must be positive. Once the updated point \mathbf{x}_r fulfills $f(\mathbf{x}_1) \leq f(\mathbf{x}_r) < f(\mathbf{x}_n)$, the current worst point will be replaced by \mathbf{x}_r for the new iteration until the termination criteria are met. In case of $f(\mathbf{x}_r) < f(\mathbf{x}_1)$, the current best point \mathbf{x}_1 will be expanded as

$$\mathbf{x}_e = \mathbf{x}_0 + \beta(\mathbf{x}_r - \mathbf{x}_0) \quad (\beta > 1) \quad (42)$$

Likewise, \mathbf{x}_{n+1} will be replaced by \mathbf{x}_e if $f(\mathbf{x}_e) < f(\mathbf{x}_r)$. However, if $f(\mathbf{x}_r) \geq f(\mathbf{x}_n)$, the expansion will be skipped and the point will be contracted as

$$\mathbf{x}_c = \mathbf{x}_0 + \chi(\mathbf{x}_{n+1} - \mathbf{x}_0) \quad (0 < \chi \leq 0.5) \quad (43)$$

Fast nonlinear mechanical decoupling for asphalt-based composites

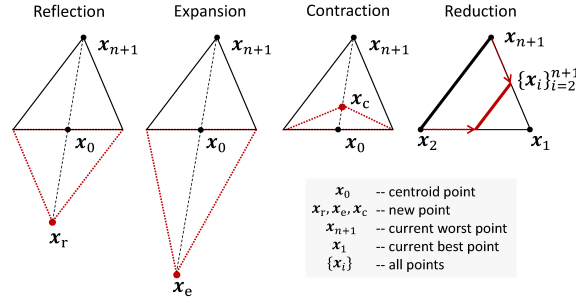


Figure 13: Geometric operations in Nelder-Mead (N-M) model, i.e., reflection, expansion, contraction and reduction, which are visualized as a set of tentative movements (in red) used to be mapped on top of the optimization space parameters.

The worst point is replaced with \mathbf{x}_c when $f(\mathbf{x}_c) < \mathbf{x}_{n+1}$. Otherwise, the reduction operation will be conducted, where all the points ($\{\mathbf{x}_i\}, i=2, \dots, n+1$) except \mathbf{x}_1 are reduced and a new iteration begins afterward:

$$\{\mathbf{x}_i\}_{i=2}^{n+1} = \{\mathbf{x}_1\} + \theta (\{\mathbf{x}_i\}_{i=2}^{n+1} - \{\mathbf{x}_1\}) \quad (0 < \theta < 1) \quad (44)$$

According to the standard N-M algorithm, the coefficients of each tentative movement, namely reflection (α), expansion (β), contraction (χ) and reduction (θ) are set as 1, 2, 0.5 and 0.5, respectively. It should be noted that a series of conditions must be fulfilled during the optimization to ensure the physical meaning of the parameters. Thus, the N-M model is enriched with constraints by setting additional rules on the parameters. The pseudocode of this in-house multi-constrained implementation is given in Algorithm 2. After the operation of each movement, “Check_Condition” is run to check if the physical meaning of each updated parameter can be fulfilled, the pseudocode of which is given in Algorithm 3. It should be noted that the algorithm will reduce the coefficient by $1/ndiv$ within the current movement once the physical conditions cannot be met. Here, $ndiv$ is the maximum number of trials in each operation, which is set as 10 in this study. After $ndiv$ failed trials, the algorithm will skip the current operation and move to the next one.

On the other hand, it is expected that the constitutive model using the optimized material parameters was able to capture the features of the stress-strain response under different loading conditions. Therefore, the algorithm has been designed to make use all the experimental monotonic stress-strain curves at different strain rates in both compression and tension. To do this, the objective function is expanded as a result of multiple functions with user-defined weights. The same set of updated parameters are then used to get the numerical results under m loading conditions simultaneously. The comparison between the experimental and numerical results under different conditions is conducted in each movement to evaluate the suitability of the parameters. The termination criteria is defined as no improvement after a user-defined number of iterations with a tolerance δ . The modified N-M model is developed in the programming language Python and it is fully compatible to be executed in Abaqus/CAE environment [64].

5.2. MPI execution

A single element (SE) test using the E-VP-VD model of sec. 4 is developed for the MPI using FEM. With the simple geometry of a unit cube, the intrinsic material response can be studied reliably and efficiently. The details of the boundary conditions are illustrated in Fig. 14, where the displacement of the bottom surface (S_{bot}) is only restricted in the loading direction along the y-axis. A uniaxial compressive or tensile load is applied on the reference point (RP) which is connected to the upper surface of the specimen (S_{top}) by an equation constraint as it is detailed on the right side of Fig. 14. To allow transverse deformations due to Poisson effect, only the displacements of the edges labeled as E_{OX} and E_{OZ} are restricted along the directions OZ and OX, respectively. In every iteration, the optimization algorithm requires to run the finite element calculation of this SE test under different loading conditions simultaneously. After finalizing the FEM calculation, stress-strain curve is post-processed from the simulation and it is compared with the test results for each iteration. The average area difference between the experimental and numerical stress-strain curves

Algorithm 2: Modified N-M model with multi-constraints for simultaneous optimization.

```

1  ▶ Initialization:
2  ▷ Generate the initial simplex:  $\mathbf{x}_i, i \in [1, n + 1]$ 
3  ▷ Compute the multiple objective functions:
4   $f(\mathbf{x}) \leftarrow$  Eq. 45
5  while termination criteria not fulfilled do
6  ▶ Sort solution:
7   $f(\mathbf{x}_i) \leftarrow$  Eq. 40
8  ▶ Centroid:
9  Compute:  $\mathbf{x}_0$ 
10 ▶ Reflection:
11  $\mathbf{x}_r \leftarrow$  Eq. 41
12  $f(\mathbf{x}_r) \leftarrow$  Check_Condition( $\alpha, \mathbf{x}_r$ )
13 if  $f(\mathbf{x}_1) \leq f(\mathbf{x}_r) < f(\mathbf{x}_n)$  then
14 |  $\mathbf{x}_{n+1} \leftarrow \mathbf{x}_r$ 
15 else if  $f(\mathbf{x}_r) < f(\mathbf{x}_1)$  then
16 | ▶ Expansion:
17 |  $\mathbf{x}_e \leftarrow$  Eq. 42
18 |  $f(\mathbf{x}_e) \leftarrow$  Check_Condition( $\beta - 1, \mathbf{x}_e$ )
19 | if  $f(\mathbf{x}_e) < f(\mathbf{x}_r)$  then
20 | |  $\mathbf{x}_{n+1} \leftarrow \mathbf{x}_e$ 
21 | else
22 | |  $\mathbf{x}_{n+1} \leftarrow \mathbf{x}_r$ 
23 | end
24 else
25 | ▶ Contraction:
26 |  $\mathbf{x}_c \leftarrow$  Eq. 43
27 |  $f(\mathbf{x}_c) \leftarrow$  Check_Condition( $\chi, \mathbf{x}_c$ )
28 | if  $f(\mathbf{x}_c) < f(\mathbf{x}_{n+1})$  then
29 | |  $\mathbf{x}_{n+1} \leftarrow \mathbf{x}_c$ 
30 | else
31 | ▶ Reduction:
32 |  $\{\mathbf{x}_i\}_{i=2}^{n+1} \leftarrow$  Eq. 44
33 | for  $i \leftarrow 2$  to  $n + 1$  do
34 | |  $f(\mathbf{x}_i) \leftarrow$  Check_Condition( $\theta, \mathbf{x}_i$ )
35 | end
36 end
37 end
38 end

```

are used as the evaluation criterion of the optimization, which is defined as

$$f(\mathbf{x}) = \frac{\sum_{k=1}^m f_k(\mathbf{x})w_k}{\sum_{k=1}^m w_k} \quad (45)$$

$$f_k(\mathbf{x}) = \int |h_k(\mathbf{x}, \varepsilon) - g_k(\mathbf{x}, \varepsilon)| d\varepsilon$$

where h_k and g_k are the k -th numerical and experimental curves, respectively, and m is the total number of loading conditions (i.e., $m=10$ in this study). Here, all the conditions are considered having the same weight ($w_k = 1$). The algorithm terminates automatically when $f(\mathbf{x})$ no longer improve for 20 iterations with a tolerance of 10^{-6} .

Algorithm 3: Check_Condition.

```

► Input:  $z, \mathbf{x}$ 
1 while  $z > 0$  do
  ► Check condition:
2   ► Physical condition of parameters
   // if VP:  $E \geq 0, C_1 \geq 0, C_2 \leq 0, m > 0, \tau_B \geq 0$ 
   // if VD:  $d_\infty > 0, \eta > 0$ 
3   if fulfill condition then
4     Simultaneous Simulation:  $f(\mathbf{x}) \leftarrow \text{Eq. 45}$ 
5     break
6   else
7      $z = z - z/ndiv$ 
8   end
9 end
10 return  $f(\mathbf{x})$ 

```

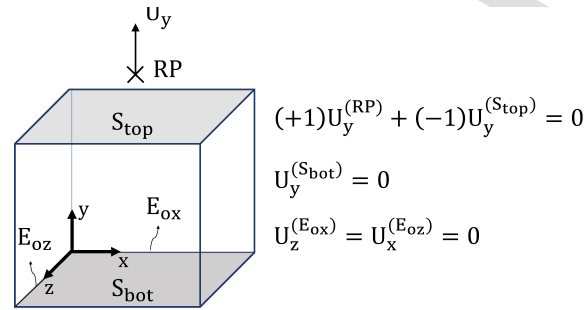


Figure 14: Schematic representation of the Single Element (SE) model to be run in the FEM solver Abaqus. The reference point (RP), the surfaces (S_{top} and S_{bot}) and the edges (E_{ox} and E_{oz}) where the boundary conditions are applied, are highlighted. The restricted boundary element and the equation constraint connecting RP to S_{top} are given on the right side.

5.3. Stage I: Identification of Elastic-ViscoPlastic Parameters

The pre-peak part ($\varepsilon < \varepsilon_{peak}$) of the stress-strain curve from the monotonic test is selected for the MPI of the E-VP model. It is worth mentioning that the compression and tension test results at different strain rates are used simultaneously during the MPI. To be specific, the updated parameters are used to run the simulations in condition of different strain rates and different loading directions at the same time in each iteration, and then the average difference $diff=f(\mathbf{x})$ is calculated by comparing the numerical and experimental results in each loading condition. Therefore, the final optimized parameters are more general since they cover all the loading conditions studied in the experimental analysis.

After some trials, the initial values of the parameters are firstly determined as $E=300$ MPa, $C_1=0.01$, $C_2=-0.24$, $\tau_B=1.4$ MPa, $m=1.5$ and $\xi=0.7$. It takes 123 s to run 10 simulations in each iteration on a workstation DELL PowerEdge T630 equipped with 2 Intel Xeon CPU without parallelization. The change of $diff$ with iterations is given in Fig. 15, which shows a good convergence ratio. The optimal values of the E-VP parameters are obtained at the 364th iteration and it is listed in Table 4. The optimization result is shown in Fig. 16 together with the error band of the experimental results represented in shadow.

In general, the numerical results using the optimized material parameters show consistency with the experimental results. The model is able to capture the rate-dependent and C-T asymmetric behavior. Albeit the model predictions under tensile load are more conformal to the experimental tensile results, the compressive ones seem to show less agreement with the real test. The mismatch can be caused by the underestimation of the experimental uncertainties as

Fast nonlinear mechanical decoupling for asphalt-based composites

Table 4

Results of the Modified N-M Optimization.

Parameters	E (MPa)	C_1	C_2	τ_B (MPa)	m	ξ	$diff$
Optimal values	293.8	0.01	-0.36	1.58	1.68	0.84	0.14

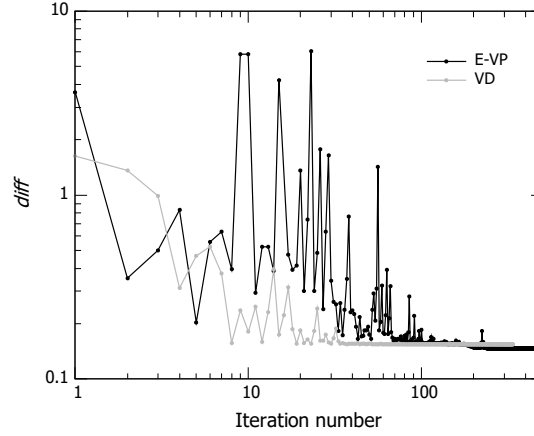


Figure 15: History of the average difference ($diff$) between the experimental and numerical stress-strain curves during optimization. For a better visualization of the convergence rate, a log-log representation is provided. The optimal values of the E-VP (in black) and VD (in gray) parameters are obtained at the 364th and 69th iteration, respectively.

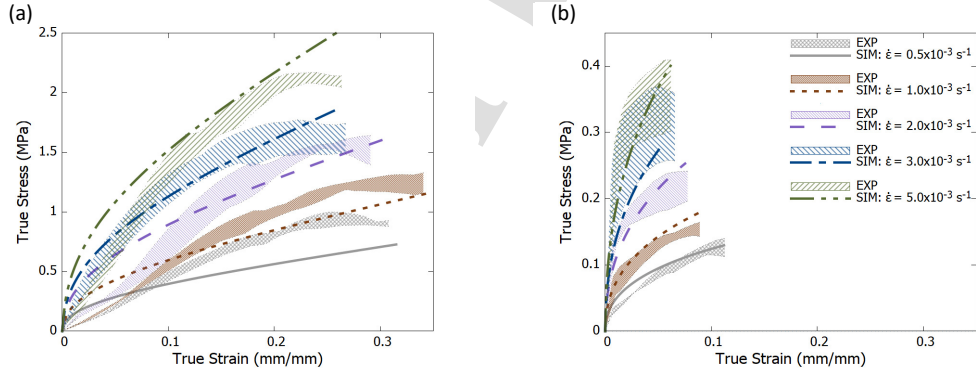


Figure 16: Numerical results (SIM) of the pre-peak part ($\epsilon < \epsilon_{peak}$) at different strain rates using the optimized E-VP material parameters: (a) compression; (b) tension. The shaded area represents the experimental error band obtained from the testing campaign. Please note that the legend is valid for both plots.

discussed in Section 3.1.

Despite the experimental difficulties to adjust the model parameters under low compressive strain rate, the optimization result reveals that the proposed modified N-M method can efficiently and decently identify multiple material parameters with constraints.

5.4. Stage II: Identification of ViscoDamage Parameters

With the determined EVP parameters, the VD parameters can be identified based on the post-peak part ($\epsilon > \epsilon_{peak}$) of the stress-strain curve from the monotonic tensile test. The initial values of the damage parameters are firstly

Table 5

Results of the Modified N-M Optimization.

Parameters	\dot{d}_∞ (s ⁻¹)	η	$diff$
Optimal values	10 ⁶	2.064	0.155

determined as $\dot{d}_\infty=10^6$ s⁻¹ and $\eta=1.85$ based on some trials. It takes 78.5 s to run 5 simulations for each iteration. The history of $diff$ is shown in Fig. 15. The optimal values of the VD parameters are obtained at the 69th iteration and it is listed in Table 5. The numerical and experimental results are presented in Fig. 17.

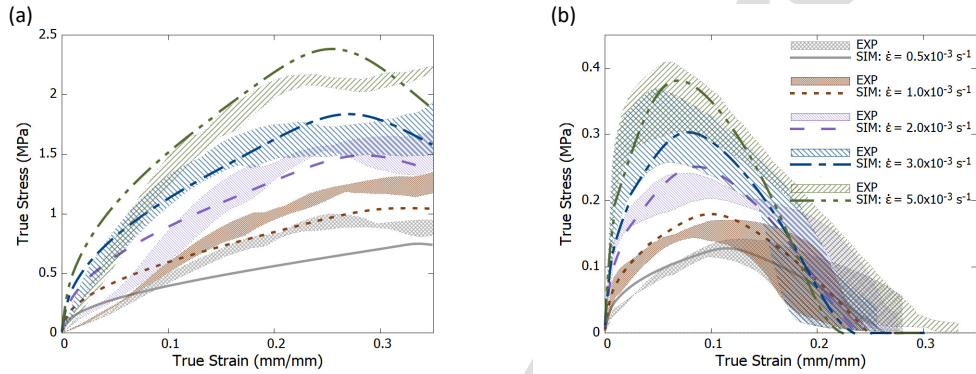


Figure 17: Numerical results (SIM) at different strain rates using the full set of the optimized parameters of the E-VP-VD model: (a) compression; (b) tension. The shaded area represents the experimental error band obtained from the testing campaign. Please note that the legend is valid for both plots.

Fig. 17 shows the comparison between the numerical and experimental results. The rate-dependency and C-T asymmetry can be satisfactorily captured by the proposed full E-VP-VD model. The peak stress is positively correlated with the strain rate, while the strain at the peak shows the opposite. Besides, the rate-dependent damage initiation and evolution are properly predicted. When the strain rate is higher, the softening curve is steeper, indicating a more pronounced damage evolution.

5.5. Verification via LUR test result

Due to the uncertainties like friction and aggregate interlocking during the compressive loading, only the tensile LUR test results are adopted for the verification of the proposed model.

The virtual tensile LUR test at two representative (the lowest and the highest) strain rates, 0.5 and 5 ($\times 10^{-3}$ s⁻¹), are conducted using the validated material model, where the user-defined subroutine VUAMP is developed to apply the same cyclic LUR load according to the experiment. The comparison between the numerical and experimental results is shown in Fig. 18. The overlapping of the unloading-reloading curves suggests that the accumulation of plastic strain and the softening process can be well predicted by the model. It should be noted that the disagreement of the initial part between the numerical and experimental curves is within the acceptable error band, which is mainly caused by factors like temperature difference, operation error and initial material defects.

In addition, the comparison of the stress-strain response between the monotonic and the LUR loading is given in Fig. 19. Fig. 19a shows that the numerical softening curves of the LUR results are lower than those of the monotonic results, which agrees well with the experimental results shown in Fig. 19b. The difference between the softening curves indicates more energy dissipation under LUR loading during the damage process when the strain rate is larger, which is also captured by the numerical model. It has been checked that larger number of the LUR cycles (N_{LUR}) leads to a larger amount of dissipated energy accelerating the degradation process in the material, as shown in Fig. 20. With the increase of N_{LUR} , the average brittleness increases, leading to a faster failure. Therefore, the model has the potential to be extended to understand the correlation between the cyclic frequency and the intrinsic degradation underwent by the material in a fatigue scenario.

Fast nonlinear mechanical decoupling for asphalt-based composites

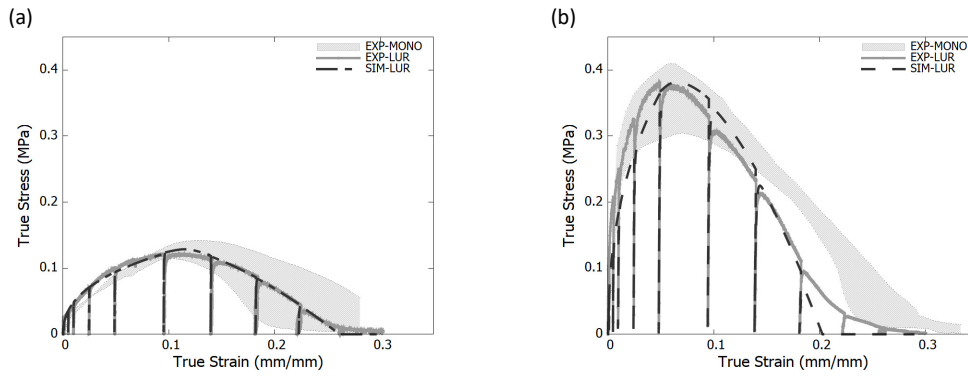


Figure 18: Comparison between numerical and experimental LUR tensile test results at the lowest and highest strain rates: (a) $\dot{\epsilon} = 0.5 \times 10^{-3} \text{ s}^{-1}$; (b) $\dot{\epsilon} = 5 \times 10^{-3} \text{ s}^{-1}$. The shaded error band of the experimental results (MONO) is provided for a better comparison.

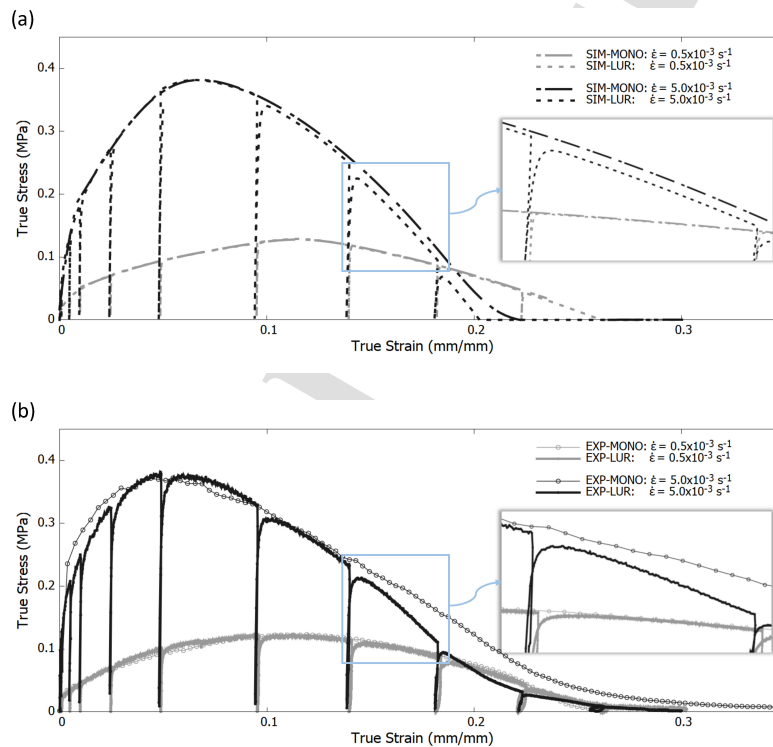


Figure 19: Comparison between monotonic and LUR test results at the lowest ($0.5 \times 10^{-3} \text{ s}^{-1}$) and highest ($5 \times 10^{-3} \text{ s}^{-1}$) strain rates: (a) simulation; (b) experiment. The zoomed area shows the difference of softening curves between the LUR and monotonic results.

The above results show that the proposed material model can provide good quantitative and qualitative predictions of the stress-strain behavior under cyclic LUR loading conditions. In that sense, it is important to highlight that the model parameters require only simple monotonic uniaxial tests in compression and tension, which makes it practical and suitable from the experimental point of view. The consistency between the experimental and numerical LUR results provides a good validation and verification of the constitutive model and the optimization algorithm proposed

Fast nonlinear mechanical decoupling for asphalt-based composites

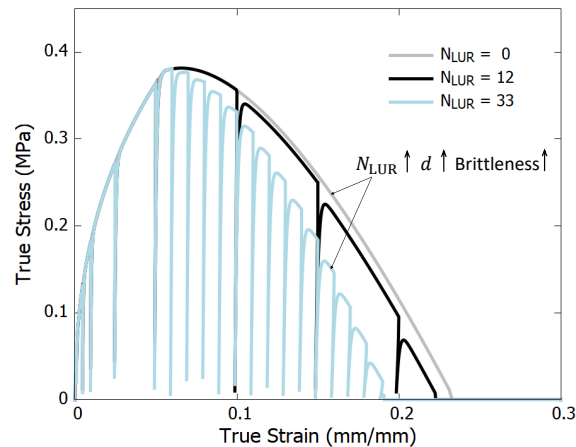


Figure 20: Effect of LUR cycles on the stress-strain response at a representative strain rate ($5 \times 10^{-3} \text{ s}^{-1}$).

in this study.

6. Discussion

This research proposes a comprehensive and fast modeling approach by combining and modifying key existing models but aiming at simplifying and minimizing the cost of experimental testing and without losing reliability on the results. Unlike other more sophisticated constitutive modeling approaches, the present reduces the number of material parameter to be characterized without losing sight on their physical interpretation. This feature is essential to make this approach practical in realistic industrial scenarios, where the access to advanced testing instruments or assuming high computational costs can seriously affect the productivity.

Asphalt matrix results as a very suitable candidate to demonstrate the capabilities of the framework. The comparison between the numerical and experimental results suggests that features such as rate-dependency, pressure dependency (compression-tension asymmetry), and the slope during unloading can be well captured by the proposed material model. Moreover, the model can capture the energy dissipation during LUR loading, which is consistent with the experimental observations. To sum up, the proposed constitutive model is able to capture the material behavior qualitatively and quantitatively. Nevertheless, although the proposed model and the parameter identification procedure are validated against uniaxial loading-unloading-reloading tests, the validity for more complex multiaxial stress states is currently under investigation in order to conclude whether monotonic uniaxial tests could be truly sufficient to fully characterize materials with these type of mechanical features. For instance, the damage initiation and evolution law in shear is by far out of the scope of this paper but still remains to be studied. The current model allows for an extension of damage in shear, which can be coupled with the developed damage model in extension. In that sense, the test campaign in torsion will be useful to verify this approach.

On the other hand, the proposed model only aims at solving an isothermal problem at 24°C , which cannot be applied for now in a non-steady thermal condition. A preliminary experimental analysis is done to check the thermal sensitivity of the asphalt material under this research. The stress-strain responses at a strain rate of $3 \times 10^{-3} \text{ s}^{-1}$ in different thermal conditions ($T=21,23,24$ and 27°C) are shown in Fig. 21.

It is found that when the temperature changes in 1°C the slope and the peak of the stress-strain curves can vary remarkably. In other words, temperature difference can cause a certain amount of variation in the experimental results. Therefore, it is of great importance to extend the current constitutive model to incorporate the thermomechanical coupling. A modified model considering thermal effects on the stiffness, creep rate and damage evolution is currently under development and it will be presented in a forthcoming work.

This study is currently being extended to include thermal effects and incorporated in multiscale analysis. The proposed framework proves its value suitable to fulfill several important industrial demands, such as (i) low number

Fast nonlinear mechanical decoupling for asphalt-based composites

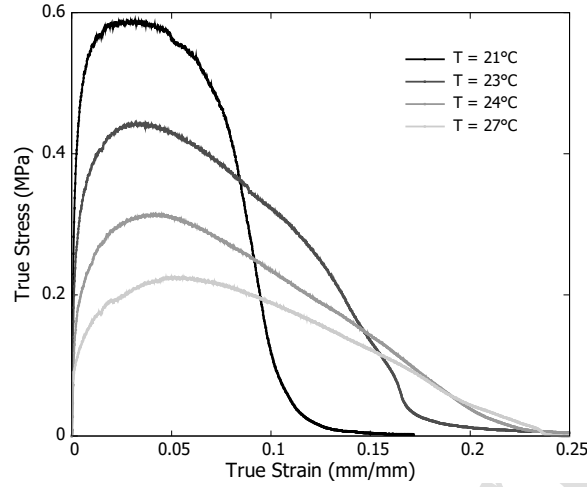


Figure 21: Stress-strain curves at different temperature (21, 23, 24, 27°C). The specimens are all tested at $\dot{\epsilon}=3\times 10^{-3} \text{ s}^{-1}$.

of cost-effective experimental tests, (ii) minimum number of parameters, (iii) model modularity allowing for easy and comprehensive way to add new mechanic features, and (iv) objective and efficient quantification of the material parameters that improves industrial competitiveness in developing new materials.

7. Conclusions

This study develops a combined experimental-numerical framework to identify and to efficiently capture the non-linear global mechanical response of materials composed of stiff inclusions embedded in a soft matrix. A highly nonlinear asphalt matrix used in road engineering is chosen to prove the feasibility of the framework. This work integrates an experimental setup, a flexible constitutive model and an efficient MPI method. Based on this study, the following conclusions can be drawn.

A notorious nonlinear mechanical behavior is experimentally observed within the strain rate ranging from 0.5 to $5 (\times 10^{-3} \text{ s}^{-1})$ under both compression and tension. In particular, the stiffness and strength of the asphalt matrix in compression are around 3 and 5 times more than those in tension, respectively. The proposed pressure-dependent viscoplastic component and the damage evolution law successfully capture the rate-dependency and the compression-tension asymmetry in the mechanical response and failure mode. The model can be implemented for any FEM-based software using implicit or explicit solver. The damage initiation shows a logarithmic dependency of the strain at peak stress and the strain rate. The extended definition of ϵ_{peak} indirectly proves the hypothesis of interlocking and reveals a contributory cause of the compression-tension asymmetry.

The gradient-less-based MPI algorithm allows for approaching highly non-linear functions with multiple variables and user-defined constrains. Most importantly, the MPI process only requires a minimum set of monotonic tests in compression and tension and can satisfactorily predict the cyclic loading-unloading-reloading response using the achieved parameters. This outcome proves the robustness of the approach to predict the mechanical behavior under complex loads and shows the potential of the model to be extended to understand the intrinsic degradation in a fatigue scenario.

Appendices

A. Stiffness degradation calculation from LUR tests

The procedure to calculate the stiffness change and the enclosed area in every LUR loop consists of three basic functions. For the sake of completeness, the pseudo code of the procedure is provided, which can be straightforwardly transcribed in Python programming language. The fragment of Algorithm 4 describes the function of the main program. The list *data* stores all the file names containing the true stress-strain curve in a simple two column format (line

Fast nonlinear mechanical decoupling for asphalt-based composites

1). This list is looped, where the every stress-strain is extracted and stored in *curve* (line 2). For every curve, any existing self-intersection is detected and stored in two lists, *cip* and *iss* (line 4). The list *cip* records the coordinates of the intersection points for the current curve, whilst *iss* records the indexes of the intersecting segment in that curve. The size of *iss* provides the number of LUR cycles in *curve* (line 6). After that, every LUR cycle of *curve* is iterated (line 7). Within this loop, using the indexes recorded by *iss*, the piece of *curve* corresponding to every LUR cycle is storage in *loop*. Then, the area enclosed by the cycle, its slope and the lower strain value are easily retrieved.

Algorithm 4: Main function to analyze LUR $\sigma - \varepsilon$ curves.

```

▶ Input: file names list of  $\sigma - \varepsilon$  curves
1  data  $\leftarrow$  ["test1.dat", ..., "testn.dat"]
▶ Sweep all files
2  for i  $\leftarrow$  1 to n do
    ▶ Read file and load  $\sigma - \varepsilon$  curve:
3  curve  $\leftarrow$  get_curve(data[i])
    ▶ Detect existing self-intersections:
4  cip, iss  $\leftarrow$  Compute_Self_Intersections(curve)
    ▶ Create empty array to store results:
5  results  $\leftarrow$  []
    ▶ Sweep along the detected LUR loops
    ▶ Number of detected loops:
6  nloop  $\leftarrow$  size(iss)
7  for k  $\leftarrow$  1 to nloop do
    ▶ Extract index interval of k-th LUR loop:
8  kini = iss[k][0]
9  kfin = iss[k][1]
    ▶ Extract piece of  $\sigma - \varepsilon$  curve corresponding to the k-th loop:
10 loop  $\leftarrow$  [curve[kini] : [kfin]]
    ▶ Enclosed area: integral Simpson Rule
    ▶ Plastic strain: lowest  $\varepsilon$  value
    ▶ LUR stiffness: slope formed by highest and lowest points
    ▶ Store in results
11 end
12 end
▶ Save results in text file

```

The fragment of Algorithm 5 describes the procedure to detect a self-intersection in the curve. Every pair of segments is extracted from *curve* (lines 2, 3 and 5, 6) and it is checked whether they intersect or not (line 7). In case of intersecting, the coordinates of the crossing point and the segment's indexes are stored in *cip* and *iss*, respectively (lines 8, 9). Algorithm 6 performs the calculation of the segments intersection. This procedure is based on explicitly constructing the equations of both segments and determine if a common point exists. If the segments are parallel (line 5, 6) or the intersecting point lays outside the minimum bounding box defined by them (line 12), this function returns a signal (line 15) to force Algorithm 5 to start a new iteration by using two new pair of segments. Otherwise, the coordinates of the intersecting point are returned to Algorithm 5 (line 13).

B. Parameter sensitivity study

The parameter sensitivity analysis of E-VP model under LUR loading is summarized in Fig 22, where the pressure-dependency is not included ($\xi=0$) for the sake of simplicity. The results show that the general slope (stiffness) of the stress-strain curve is sensitive to all the parameters, whereas the dissipation area is controlled by τ_B and *m*. Moreover, the rate-dependency can be captured by this model, as is shown in Fig 23.

Algorithm 5: Compute_Self_Intersections. This function returns the intersecting segments to each other in a curve.

```

► Input: curve  $\leftarrow [p_1, \dots, p_N]$  with  $p_k = [x_k, y_k]$ 
► Output:  $cip, iis$ 
    $cip$ : coordinates of intersection points
    $iis$ : indexes of intersecting segments
► Initialization: create empty arrays
    $cip \leftarrow []$ 
    $iis \leftarrow []$ 
1 for  $i \leftarrow 1$  to  $N$  do
2    $p_A \leftarrow \text{curve}[i]$ 
3    $p_B \leftarrow \text{curve}[i + 1]$ 
4   for  $j \leftarrow i + 2$  to  $N$  do
5      $p_C \leftarrow \text{curve}[j]$ 
6      $p_D \leftarrow \text{curve}[j + 1]$ 
7      $p_I \leftarrow \text{Compute\_Intersection}(p_A, p_B, p_C, p_D)$  if  $p_I \neq \text{False}$  then
8        $cip.append(p_I)$ 
9        $iis.append([i + 1, j + 1])$ 
10       $i = j + 2$ 
11       $j = N$ 
12    end
13  end
14 end
15 return  $cip, iis$ 

```

Algorithm 6: Compute_Intersection. This function returns coordinate of two intersecting segments.

```

► Input:  $p_A, p_B, p_C, p_D$ 
► Define two segments:
1    $S_{AB} \leftarrow [p_A, p_B]$ 
2    $S_{CD} \leftarrow [p_C, p_D]$ 
► Construct equation of segments,  $S_{AB}, S_{CD}$ :
3    $S_{AB}(t) \leftarrow M_{AB}t + Y_{AB}$ 
4    $S_{CD}(t) \leftarrow M_{CD}t + Y_{CD}$ 
► Check segments no parallel:
5 if  $|M_{AB} - M_{CD}| < 10^{-8}$  then
6   return False
7 end
► Compute intersection point  $p_I = [x_I, y_I]$ :
8    $x_I \leftarrow (Y_{CD} - Y_{AB}) / (M_{CD} - M_{AB})$ 
9    $y_I \leftarrow M_{AB}x_I + Y_{AB}$ 
► Compute bounding box formed by  $S_{AB}, S_{CD}$ :
10   $BB \leftarrow [[\min\{x_i\}, \min\{y_i\}], [\max\{x_i\}, \max\{y_i\}]]$ 
11   $x_i, y_i \in \{p_k\}$  with  $k = A, B, C, D$ 
► Check intersection inside bounding box:
12 if  $p_I \in BB$  then
13   return  $p_I$ 
14 else
15   return False
16 end

```

Fast nonlinear mechanical decoupling for asphalt-based composites

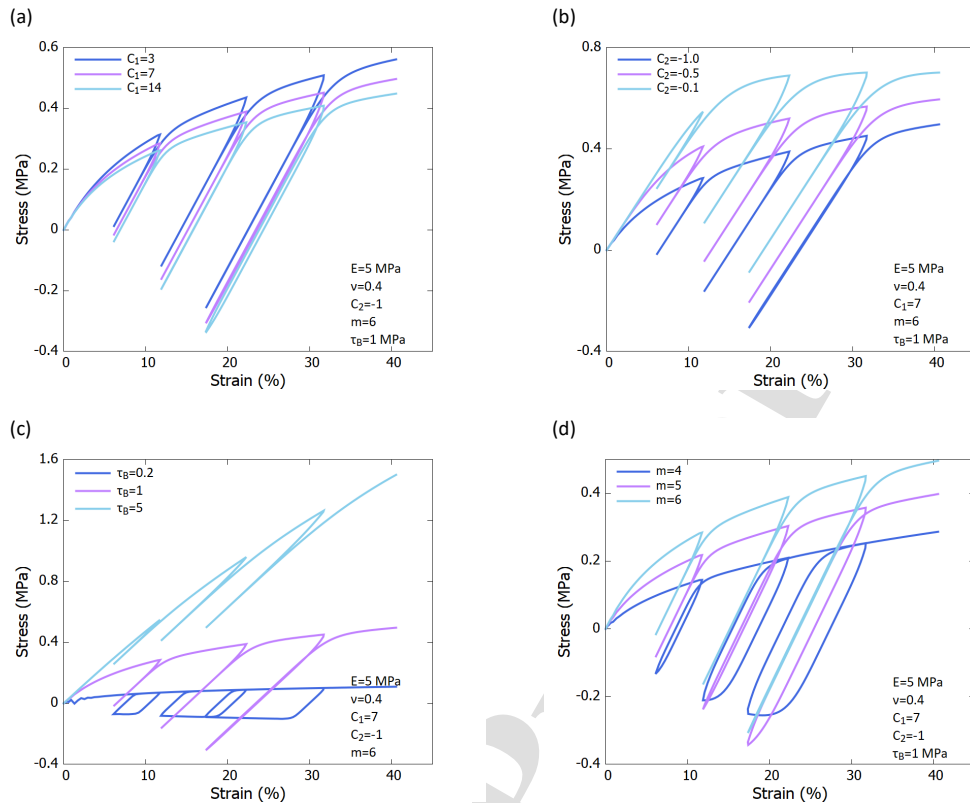


Figure 22: Sensitivity analysis of elasto-viscoplastic parameters on the stress-strain response: (a) effect of C_1 ; (b) effect of C_2 ; (c) effect of τ_B ; (d) effect of m . It should be noted that the pressure-dependency is not included ($\xi=0$).

Declaration of competing interest

The authors declare that they have no known financial or personal interest or belief that could affect their objectivity. The authors confirm explicitly that no conflicts of interest exist.

Authors' contributions

Z. Dai: Conceptualization, Investigation, Methodology, Software, Data curation, Formal analysis, Validation, Writing - Original Draft.

V. Laheri: Formal analysis, Validation, Software, Writing - Review & Editing.

X. Zhu: Conceptualization, Resources, Funding, Writing - Review & Editing, Supervision.

F. A. Gilibert: Conceptualization, Methodology, Software, Data curation, Formal analysis, Writing - Review & Editing, Supervision.

All authors read and approved the final manuscript.

Acknowledgments

The work described in this paper is supported by the National Natural Science Foundation of China (Nos. 51922079, 61911530160), Shanghai Pujiang Program, the Fundamental Research Funds for the Central Universities, and by the Special Research Fund (BOF, "Bijzonder Onderzoeksfonds") of Ghent University (BOF.STG.2018.0030.01). We sincerely appreciate all the valuable comments and suggestions by the reviewers, which helped to substantially improve the manuscript.

Fast nonlinear mechanical decoupling for asphalt-based composites

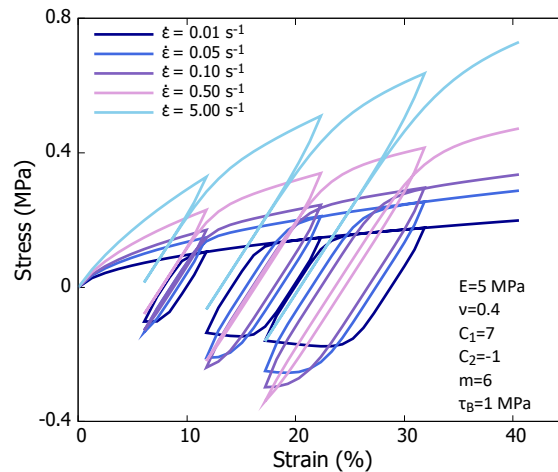


Figure 23: Effect of strain rate on the stress-strain response.

References

- [1] K. Xu, W. Chen, L. Liu, Z. Zhao, and G. Luo. A hierarchical multiscale strategy for analyzing the impact response of 3d braided composites. *International Journal of Mechanical Sciences*, 193:106167, 2021.
- [2] N. Arora, Y. Xiang, and S. Rudykh. Multiscale analysis of elastic waves in soft materials: From molecular chain networks to fiber composites. *International Journal of Mechanical Sciences*, 200:106433, 2021.
- [3] K. Xu, W. Chen, L. Liu, Z. Zhao, and G. Luo. Numerical implementation, comparison and validation of a pressure dependent model for polymer composites. *International Journal of Mechanical Sciences*, 212:106818, 2021.
- [4] V. Laheri, P. Hao, and F. A. Gilabert. Efficient non-iterative modelling of pressure-dependent plasticity using paraboloidal yield criterion. *International Journal of Mechanical Sciences*, 217:106988, 2022.
- [5] M. R. Islam, H. M. Faisal, and R. A. Tarefder. Determining temperature and time dependent Poisson's ratio of asphalt concrete using indirect tension test. *Fuel*, 146:119–124, 2015.
- [6] S. Pirmohammad, M. Abdi, and M. R. Ayatollahi. Mode II fracture tests on asphalt concrete at different temperatures using semi-circular bend specimen loaded by various types of supports. *Theoretical and Applied Fracture Mechanics*, 116:103089, 2021.
- [7] B. G. Liu, K. Kandan, H. N. G. Wadley, and V. S. Deshpande. High strain rate compressive response of ultra-high molecular weight polyethylene fibre composites. *International Journal of Plasticity*, 122:115–134, 2019.
- [8] D. L. Grote, S. W. Park, and M. Zhou. Dynamic behavior of concrete at high strain rates and pressures: I. experimental characterization. *International Journal of Impact Engineering*, 25:869–886, 2001.
- [9] X. Gong, P. Romero, Z. Dong, and D. S. Sudbury. The effect of freeze-thaw cycle on the low-temperature properties of asphalt fine aggregate matrix utilizing bending beam rheometer. *Cold Regions Science and Technology*, 125:101–107, 2016.
- [10] X. Wang, J. Ren, X. Gu, N. Li, Z. Tian, and H. Chen. Investigation of the adhesive and cohesive properties of asphalt, mastic, and mortar in porous asphalt mixtures. *Construction and Building Materials*, 276:122255, 2021.
- [11] Z. Dai, V. Laheri, X. Zhu, and F. A. Gilabert. Experimental study of Compression-Tension asymmetry in asphalt matrix under Quasi-static and dynamic loads via an integrated DMA-based approach. *Construction and Building Materials*, 283:122725, 2021.
- [12] J. Vincent. *Chapter One. Basic Elasticity and Viscoelasticity*. Princeton University Press, 2012.
- [13] R. Schapery. Stress analysis of viscoelastic composite materials. *Journal of Composite Materials*, 1(3):228–267, 1967.
- [14] R. Schapery. On the Characterization of Nonlinear Viscoelastic Materials. *Polymer Engineering & Science*, 9:295–310, 1969.
- [15] W. Huang, X. Zhang, and Y. Yin. An image-based finite element approach for simulating viscoelastic response of asphalt mixture. *Advances in Materials Science and Engineering*, 2016:e7428623, 2016.
- [16] Y. Sun, Z. Zhang, X. Wei, C. Du, M. Gong, J. Chen, and H. Gong. Mesomechanical prediction of viscoelastic behavior of asphalt concrete considering effect of aggregate shape. *Construction and Building Materials*, 274:122096, 2021.
- [17] F. Bai, X. Yang, and G. Zeng. A stochastic viscoelastic-viscoplastic constitutive model and its application to crumb rubber modified asphalt mixtures. *Materials & Design*, 89:802–809, 2016.
- [18] R. K. Abu Al-Rub, M. K. Darabi, S. M. Kim, D. N. Little, and C. J. Glover. Mechanistic-based constitutive modeling of oxidative aging in aging-susceptible materials and its effect on the damage potential of asphalt concrete. *Construction and Building Materials*, 41:439–454, 2013.
- [19] E. Rahmani, M. K. Darabi, D. N. Little, and E. A. Masad. Constitutive modeling of coupled aging-viscoelastic response of asphalt concrete. *Construction and Building Materials*, 131:1–15, 2017.
- [20] R. F. Landel and L. E. Nielsen. *Mechanical Properties of Polymers and Composites*. CRC Press, 1993.
- [21] C. Riccardi, A. Cannone Falchetto, M. Losa, and M. Wistuba. Back-calculation method for determining the maximum RAP content in Stone Matrix Asphalt mixtures with good fatigue performance based on asphalt mortar tests. *Construction and Building Materials*, 118:364–372,

Fast nonlinear mechanical decoupling for asphalt-based composites

- 2016.
- [22] A. S. Lodge. Constitutive equations from molecular network theories for polymer solutions. *Rheologica Acta*, 7(4):379–392, 1968.
- [23] P. J. Carreau. Rheological Equations from Molecular Network Theories. *Transactions of the Society of Rheology*, 16(1):99–127, 1972.
- [24] M. H. Wagner and H. M. Laun. Nonlinear shear creep and constrained elastic recovery of a LDPE melt. *Rheologica Acta*, 17(2):138–148, 1978.
- [25] J. Stastna, K. Jorshari, and L. Zanzotto. Nonlinear dynamic moduli in asphalt. *Materials and Structures*, 35(1):59–63, 2002.
- [26] S. Ren, X. Liu, M. Li, W. Fan, J. Xu, and S. Erkens. Experimental characterization of viscoelastic behaviors, microstructure and thermal stability of CR/SBS modified asphalt with TOR. *Construction and Building Materials*, 261:120524, 2020.
- [27] A. Bahrololoumi, V. Morovati, E. A. Poshtan, and R. Dargazany. A multi-physics constitutive model to predict hydrolytic aging in quasi-static behaviour of thin cross-linked polymers. *International Journal of Plasticity*, 130:102676, 2020.
- [28] J. Wang, L. F. Peng, Y. J. Deng, X. M. Lai, M. W. Fu, and J. Ni. A finite strain thermodynamically-based constitutive modeling and analysis of viscoelastic-viscoplastic deformation behavior of glassy polymers. *International Journal of Plasticity*, 122:135–163, 2019.
- [29] L. Al Khateeb, K. Anupam, S. Erkens, and T. Scarpas. Micromechanical simulation of porous asphalt mixture compaction using discrete element method (DEM). *Construction and Building Materials*, 301:124305, 2021.
- [30] Q. Huang, Z. Qian, J. Hu, D. Zheng, L. Chen, M. Zhang, and J. Yu. Investigation on the properties of aggregate-mastic interfacial transition zones (ITZs) in asphalt mixture containing recycled concrete aggregate. *Construction and Building Materials*, 269:121257, 2021.
- [31] P. Cao, Z. Leng, F. Shi, C. Zhou, Z. Tan, and Z. Wang. A novel visco-elastic damage model for asphalt concrete and its numerical implementation. *Construction and Building Materials*, 264:120261, 2020.
- [32] M. Gajewski and P. Langlois. Prediction of Asphalt Concrete Low-temperature Cracking Resistance on the Basis of Different Constitutive Models. *Procedia Engineering*, 91:81–86, 2014.
- [33] J. Neumann, J. W. Simon, K. Mollenhauer, and S. Reese. A framework for 3D synthetic mesoscale models of hot mix asphalt for the finite element method. *Construction and Building Materials*, 148:857–873, 2017.
- [34] B. Jahangiri, M. M. Karimi, O. Giraldo-Londoño, and W. G. Buttlar. Characterization of viscoelastic properties of asphalt mixture at low temperatures using DC(T) creep test. *Construction and Building Materials*, 298:123731, 2021.
- [35] Y. Lu and P. J. Wright. Numerical approach of visco-elastoplastic analysis for asphalt mixtures. *Computers & Structures*, 69(2):139–147, 1998.
- [36] A. V. Khokhlov. The nonlinear Maxwell-type model for viscoelastoplastic materials: simulation of temperature influence on creep, relaxation and strain-stress curves. *Vestnik Samarskogo Gosudarstvennogo Tekhnicheskogo Universiteta. Seriya Fiziko-Matematicheskie Nauki*, 21(1):160–179, 2017.
- [37] M. Pasetto and N. Baldo. Numerical visco-elastoplastic constitutive modelization of creep recovery tests on hot mix asphalt. *Journal of Traffic and Transportation Engineering (English Edition)*, 3(5):390–397, 2016.
- [38] Y. Li, X. He, H. Sun, and Y. Tan. Research on viscoelastic-plastic damage characteristics of cement asphalt composite binder. *Construction and Building Materials*, 274:122064, 2021.
- [39] N. H. T. Nguyen, H. H. Bui, J. Kodikara, S. Arooran, and F. Darve. A discrete element modelling approach for fatigue damage growth in cemented materials. *International Journal of Plasticity*, 112:68–88, 2019.
- [40] T. Nian, J. Ge, P. Li, M. Wang, and Y. Mao. Improved discrete element numerical simulation and experiment on low-temperature anti-cracking performance of asphalt mixture based on PFC2D. *Construction and Building Materials*, 283:122792, 2021.
- [41] K. Hu, C. Yu, Q. Yang, Yu. Chen, G. Chen, and R. Ma. Multi-scale enhancement mechanisms of graphene oxide on styrene-butadiene-styrene modified asphalt: An exploration from molecular dynamics simulations. *Materials & Design*, 208:109901, 2021.
- [42] S. Yang, H. Shin, and M. Cho. Contribution of oxygen functional groups in graphene to the mechanical and interfacial behaviour of nanocomposites: Molecular dynamics and micromechanics study. *International Journal of Mechanical Sciences*, 189:105972, 2021.
- [43] J. L. Chaboche. Continuum damage mechanics: Part I-general concepts. *Journal of Applied Mechanics*, 55(1):59–64, 1988.
- [44] V. P. Golub. Non-linear one-dimensional continuum damage theory. *International Journal of Mechanical Sciences*, (10):1139–1150, 1996.
- [45] K. Yun, Z. Wang, S. Ronald, and Y. Pak. An advanced continuum damage mechanics model for predicting the crack progress process based on the consideration of the influence of crack direction under quasi-static load. *International Journal of Mechanical Sciences*, 130:487–496, 2017.
- [46] M. Shakiba, M. K. Darabi, R. K. Abu Al-Rub, E. A. Masad, and D. N. Little. Microstructural modeling of asphalt concrete using a coupled moisture-mechanical constitutive relationship. *International Journal of Solids and Structures*, 51(25):4260–4279, 2014.
- [47] M. Shakiba, M. K. Darabi, R. K. Abu Al-Rub, D. N. Little, and E. A. Masad. Constitutive modeling of the coupled moisture-mechanical response of particulate composite materials with application to asphalt concrete. *Journal of Engineering Mechanics*, 141(2):04014120, 2015.
- [48] F. Praud, G. Chatzigeorgiou, J. Bikard, and F. Meraghni. Phenomenological multi-mechanisms constitutive modelling for thermoplastic polymers, implicit implementation and experimental validation. *Mechanics of Materials*, 114:9–29, 2017.
- [49] Q. Chen, G. Chatzigeorgiou, and F. Meraghni. Extended mean-field homogenization of viscoelastic-viscoplastic polymer composites undergoing hybrid progressive degradation induced by interface debonding and matrix ductile damage. *International Journal of Solids and Structures*, 210:1–17, 2021.
- [50] B. Li, Z. Zhu, J. Ning, T. Li, and Z. Zhou. Viscoelastic-plastic constitutive model with damage of frozen soil under impact loading and freeze-thaw loading. *International Journal of Mechanical Sciences*, 214:106890, 2022-01-15.
- [51] Y.R. Kim, F. A. C. de Freitas, J. S. Jung, and Y. Sim. Characterization of bitumen fracture using tensile tests incorporated with viscoelastic cohesive zone model. *Construction and Building Materials*, 88:1–9, 2015.
- [52] A. A. Alsheghri and R. K. Abu Al-Rub. Finite element implementation and application of a cohesive zone damage-healing model for self-healing materials. *Engineering Fracture Mechanics*, C(163):1–22, 2016.
- [53] L. Hakim and S. E. Mikhailov. A history-dependent cohesive zone model in elastic and visco-elastic materials under constant and variable loading. *International Journal of Mechanical Sciences*, 144:518–525, 2018.

Fast nonlinear mechanical decoupling for asphalt-based composites

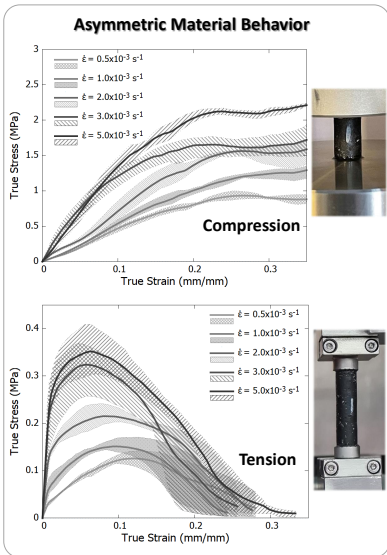
- [54] Y. Gong, Y. Hou, L. Zhao, W. Li, J. Zhang, and N. Hu. A modified mode I cohesive zone model for the delamination growth in deb laminates with the effect of fiber bridging. *International Journal of Mechanical Sciences*, 176:105514, 2020.
- [55] P. S. Pell, P. F. McCarthy, and R. R. Gardner. Fatigue of bitumen and bituminous mixes. *International Journal of Mechanical Sciences*, 3(4):247–267, 1961.
- [56] S. Benkabouche, H. Guechichi, A. Amrouche, and M. Benkhettab. A modified nonlinear fatigue damage accumulation model under multiaxial variable amplitude loading. *International Journal of Mechanical Sciences*, 100:180–194, 2015.
- [57] J. Zhang, Z. Li, H. Chu, and J. Lu. A viscoelastic damage constitutive model for asphalt mixture under the cyclic loading. *Construction and Building Materials*, 227:116631, 2019.
- [58] R. Zhang, J. E. Sias, and E. V. Dave. Evaluation of the cracking and aging susceptibility of asphalt mixtures using viscoelastic properties and master curve parameters. *Journal of Traffic and Transportation Engineering (English Edition)*, 2020.
- [59] V.V. Jinescu. Critical energy approach for the fatigue life calculation under blocks with different normal stresses amplitudes. *International Journal of Mechanical Sciences*, 67:78–88, 2013.
- [60] Z. Zhang, S. Han, H. Guo, X. Han, and C. Wu. Fatigue performance evaluation of recycled asphalt fine aggregate matrix based on dynamic shear rheometer test. *Construction and Building Materials*, 300:124025, 2021.
- [61] J. Shim and D. Mohr. Rate dependent finite strain constitutive model of polyurea. *International Journal of Plasticity*, 27(6):868–886, 2011.
- [62] F. Shen, G. Kang, Y. C. Lam, Y. Liu, and K. Zhou. Thermo-elastic-viscoplastic-damage model for self-heating and mechanical behavior of thermoplastic polymers. *International Journal of Plasticity*, 121:227–243, 2019.
- [63] Y. Jeong, B. Jeon, and C. N. Tomé. Finite element analysis using an incremental elasto-visco-plastic self-consistent polycrystal model: FE simulations on Zr and low-carbon steel subjected to bending, stress-relaxation, and unloading. *International Journal of Plasticity*, 147:103110, 2021.
- [64] SIMULIA. Abaqus 2021 User Documentation. Providence, RI, USA, 2021. Dassault Systèmes Simulia Corp.
- [65] Asphalt Institute. Hma construction. manual series no. 22 (ms-22). Standard, Asphalt Institute, Lexington, KY., 2001.
- [66] C.S. Hughes. Marshall mix design criteria (no. vhtc 81-r3). Standard, Virginia Highway & Transportation Research Council, 1980.
- [67] AASHTO312: Standard test method for dynamic young's modulus, shear modulus, and poisson's ratio by impulse excitation of vibration. Standard, American Association of State Highway and Transportation Officials, Washington, DC, 2014.
- [68] X. Lu and U. Isacsson. Effect of ageing on bitumen chemistry and rheology. *Construction and Building materials*, 16:15–22, 2002.
- [69] J. Füssl, R. Lackner, J. Eberhardsteiner, and H.A. Mang. Failure modes and effective strength of two-phase materials determined by means of numerical limit analysis. *Acta Mechanica*, 195(1):185–202, 2008.
- [70] D. Liu, C. Chen, and T. Zhang. Image-based polygonal lattices for mechanical modeling of biological materials: 2d demonstrations. *ACS Biomaterials Science & Engineering*, 2021.
- [71] W. Shen, R. Dong, J. Li, M. Zhou, W. Ma, and J. Zha. Experimental investigation on aggregate interlocking concrete prepared with scattering-filling coarse aggregate process. *Construction and Building Materials*, 24(11):2312–2316, 2010.
- [72] E. H. Lee. Elastic-plastic deformation at finite strains. *Journal of Applied Mechanics*, 36(1):1–6, 1969.
- [73] M. C. Boyce, G. G. Weber, and D. M. Parks. On the kinematics of finite strain plasticity. *Journal of the Mechanics and Physics of Solids*, 37(5):647–665, 1989.
- [74] F. A. Gilibert. Modelling nonlinear material response of polymer matrices used in fiber-reinforced composites. In *Multi-Scale Continuum Mechanics Modelling of Fibre-Reinforced Polymer Composites*, pages 219–242. Woodhead Publishing, 2021.
- [75] F. A. Gilibert. An efficient anisotropization technique to transform isotropic nonlinear materials into unidirectional and bidirectional composites. *Materials & Design*, 206:109772, 2021.
- [76] M. C. Boyce, D. M. Parks, and A. S. Argon. Large inelastic deformation of glassy polymers. part I: rate dependent constitutive model. *Mechanics of Materials*, 7(1):15–33, 1988.
- [77] J. S. Bergström and M. C. Boyce. Constitutive modeling of the large strain time-dependent behavior of elastomers. *Journal of the Mechanics and Physics of Solids*, 46(5):931–954, 1998.
- [78] A. Karrech, K. Regenauer-Lieb, and T. Poulet. A damaged visco-plasticity model for pressure and temperature sensitive geomaterials. *International Journal of Engineering Science*, 49(10):1141–1150, 2011.
- [79] E. M. Arruda and M. C. Boyce. A three-dimensional constitutive model for the large stretch behavior of rubber elastic materials. *Journal of the Mechanics and Physics of Solids*, 41(2):389–412, 1993.
- [80] L. M. Kachanov. *Introduction. Mechanics of Elastic Stability*. Springer Netherlands, Dordrecht, 1986.
- [81] M. Vaz, P.A. Muñoz-Rojas, E.L. Cardoso, and M. Tomiyama. Considerations on parameter identification and material response for gurson-type and lemaître-type constitutive models. *International Journal of Mechanical Sciences*, 106:254–265, 2016.
- [82] N. Souto, A. Andrade-Campos, and S. Thuillier. A numerical methodology to design heterogeneous mechanical tests. *International Journal of Mechanical Sciences*, 107:264–276, 2016.
- [83] G. Han, J.H. Fonseca, M. Song, N. Kim, and H. Lee. Determination of plastic properties of weld metals using an optimal regression of tensile and hardness test data. *International Journal of Mechanical Sciences*, 194:106196, 2021.
- [84] J. A. Nelder and R. Mead. A Simplex Method for Function Minimization. *The Computer Journal*, 7(4):308–313, 1965.

Highlights

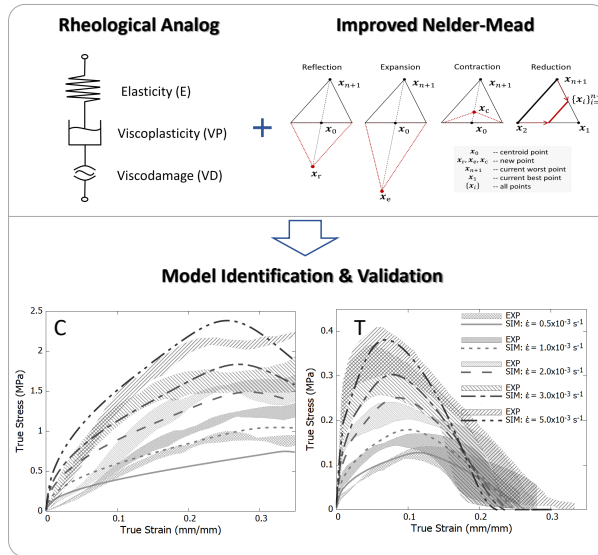
1. Pragmatic experiment-modeling framework for highly nonlinear asphalt-based composites
2. Constitutive law capturing asymmetric elasto-viscoplastic-viscodamage response
3. Experiment-based pressure- and rate-dependent damage initiation and evolution
4. Fast optimization-based algorithm for material parameter identification
5. Thorough model verification via Load-Unload-Reload tests using pure monotonic data

proof

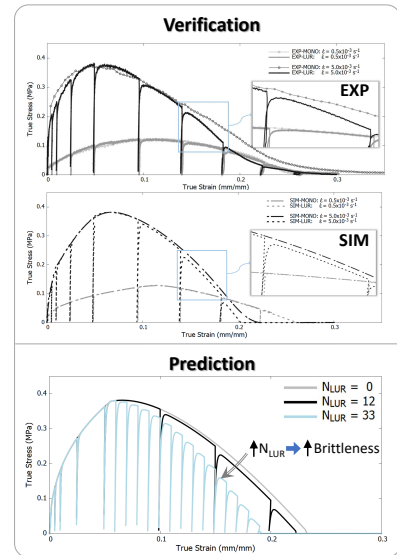
EXPERIMENT



CONSTITUTIVE MODELING



SIMULATION



Journal

Author statement

Z. Dai: Conceptualization, Investigation, Methodology, Software, Data curation, Formal analysis, Validation, Writing - Original Draft

V. Laheri: Formal analysis, Validation, Software, Writing - Review & Editing.

X. Zhu: Conceptualization, Resources, Funding, Writing - Review & Editing, Supervision.

F. A. Gilbert: Conceptualization, Methodology, Software, Data curation, Formal analysis, Writing - Review & Editing, Supervision.

Declaration of interests

The authors declare that they have no known competing financial interests or personal relationships that could have appeared to influence the work reported in this paper.

The authors declare the following financial interests/personal relationships which may be considered as potential competing interests:

Journal Pre-proof